PCCP

The basis for reevaluating the reactivity of pyrite surfaces: spin states and crystal field d-orbital splitting energies of bulk, terrace, edge, and corner Fe(II) ions

Journal:	*Physical Chemistry Chemical Physics*
Manuscript ID	CP-ART-08-2018-005459.R1
Article Type:	Paper
Date Submitted by the Author:	28-Jan-2019
Complete List of Authors:	Arumugam, Krishnamoorthy; University of Michigan, Department of Earth and Environmental Sciences; Central University of Tamil Nadu, Simulation Center for Atomic and Nanoscale MATerials (SCANMAT) Renock, Devon; Dartmouth Coll, Department of Earth Sciences Becker, Udo ; University of Michigan, Dept. of Earth and Environmental Sciences

The basis for reevaluating the reactivity of pyrite surfaces: spin states and crystal field d-orbital splitting energies of bulk, terrace, edge, and corner Fe(II) ions

Krishnamoorthy Arumugam[1]‡, Devon Renock[2], and Udo Becker[1]**

[1] Department of Earth and Environmental Sciences, University of Michigan, 1100 North University Avenue, 2534 NUB, Ann Arbor, MI 48109-1005, USA.

[2] Department of Earth Sciences, Dartmouth College, Hanover, NH 03755.

‡ Current address: National Post Doctoral Fellow, Simulation Center for Atomic and Nanoscale MATerials (SCANMAT), Central University of Tamil Nadu, Thiruvarur, Tamil Nadu, 610101, India.

***corresponding authors: Krishamoorthy Arumugam (+91 9786138099) and Udo Becker**

Phone: +1 734 615 6894

email: krish.odc@gmail.com

ubecker@umich.edu

(Electronic Supplementary Information (ESI) is available)

ABSTRACT:

Pyrite, one of the most important minerals to catalyze redox reactions in nature and a bulk low-spin Fe mineral, needs to provide high-spin Fe on surfaces to moderate spin-forbidden transitions. Here, the spin state of pyrite is investigated using density functional theory (DFT) calculations on cluster and periodic models. The energies of clusters Fe_xS_{2x} (where x = 4, 8, 16, and 32) were calculated as a function of total spin and different up/down spin configurations. The undercoordinated Fe on surfaces, edges, and corners were found to provide intermediate and high-spin Fe necessary for catalysis. Generally, the lower the crystal field splitting energy (CFSE), Δ, for a particular Fe atom, the higher is the spin density. Pyrite bulk (3D) and surfaces (2D) ([1-3] and [4]+water to mimic aqueous systems) were examined. The calculated bulk band gap (0.95 eV) is in excellent agreement with previous reports. For the [5, 6] surface, a conducting state is predicted. The calculated CFSE for bulk Fe(II) in pyrite (~2.2 eV) agrees with previous CFT results; due to surface states, this CFSE decreases to ~1 eV on [7, 8] terraces. This study highlights the importance of accurately describing the spin state of pyrite.

Keywords: Pyrite surface; Semiconducting minerals; Crystal Field Splitting Energy(CFSE); Density Functional Theory(DFT); Explicit hydration; Conductor-like

Polarizable Continuum Model(CPCM); Surface-mediated catalysis; Anti-ferromagnetic(AFM); Nano-clusters; Surface states.

1 Introduction

Redox reactions involving pyrite are the driving force behind the mobilization and biogeochemical cycling of carbon and many other elements at the Earth's surface.[9] The atomic structure and unique semiconducting properties of pyrite surface have been well described[10-14] and numerous studies show that these properties significantly influence rates and mechanisms of redox processes.[10, 15-22] However, the role of electron spin transitions in attenuating the rates of processes occurring on pyrite surfaces has not been previously investigated. In fact, there are relatively few studies of electron spin transitions occurring on mineral surfaces despite their potential to significantly affect the rates of redox processes.[22-29] Pyrite along with some iron oxides may be one of the most important minerals to catalyze redox reactions in the environment. In many cases, the actual electron transfer part of a redox reaction may be kinetically inhibited by, e.g., the spin(-forbidden) transition from paramagnetic O_2 to diamagnetic O^{2-} [12, 20, 22, 30-36]. Another example is the change from no unpaired spin in U^{6+} to two unpaired ones in U^{4+} [27]. Due to the change of electron angular momentum, these reactions would be spin-forbidden and "pre-existing" spin density on a pyrite surface or edge, or on a pyrite nanoparticle,[37] would increase the redox process by orders of magnitude. Another important process where the spin density on Fe in pyrite plays an important role for the mechanism and kinetics is pyrite oxidation.[13, 14, 37-41] For comparison, the oxidation and catalytic redox kinetics of high-spin are order of magnitude faster because all Fe(II) in pyrrhotite are in their high-spin state. [26, 40]

It is instructive to first consider what is meant by the spin state of Fe in a molecule or mineral such as pyrite. Electron spin angular momentum, *S*, is a quantum-mechanical property that can have only two values, spin "up" or spin "down" typically designated by a +1/2 and -1/2, respectively (in order to obtain an actual angular momentum, these numbers are multiplied by Planck's constant). Most silicate minerals, such as quartz and feldspar, have an equal number of +1/2 and -1/2 electrons (i.e., all electrons in molecular orbitals are paired up such that the total spin = 0). When $S = 0$, the spin multiplicity has a value of (1) based on $multiplicity = 2S + 1$. A spin multiplicity of (1) is designated as a "singlet", (2) is a "doublet", (3) is a "triplet", etc. A chemical reaction is accompanied by a redistribution of bonding electrons when chemical bonds are broken and formed. A reaction that changes the total spin multiplicity in going from reactant(s) to product(s), for example triplet to singlet, must overcome a significant activation energy barrier in order to do so. These reactions are considered "spin-forbidden" based on the law of conservation of angular momentum. Even though these reactions are not technically forbidden, often their rates are extremely slow due to the high activation energy barrier of the spin transition.[42, 43]

An important example of this phenomenon is the relatively slow rate of abiotic organic matter oxidation in the Earth's atmosphere (20% O_2 and 298 K) despite a strong thermodynamic drive to oxidize carbon to CO_2 and H_2O. Here, the paramagnetic quality of O_2 (*i.e.,* two unpaired electrons with a total $S = 1$) results in a triplet ground state [$(2S+1) = 3$]

and is thus designated $^3O_2$. The initial dissociation of $^3O_2$ during oxidation of a singlet state organic molecule is a spin-prohibited process (i.e., the triplet-to-singlet spin transition violates the law of conservation of angular spin momentum of the system) and the activation energy required to overcome the triplet-singlet spin transition has been shown to be ~100 kJ(~1 eV)/mol.[44] The prohibition comes about because angular momentum must be conserved and the coupling of electron spins with the low-spin surface is so weak that spin angular momentum is not readily exchanged in the timeframe of the O_2-surface collision. In other words, the activation barrier is determined by the magnitude of the spin-orbit coupling term (SOC) of the system's Hamiltonian.

The oxidative weathering of minerals also uses $^3O_2$ as an oxidant and is therefore potentially rate-limited by the activation of paramagnetic $^3O_2$ on the low-spin mineral surface. We highlight oxidative weathering here because of its geochemical significance, but any redox process mediated by a mineral surface is subject to kinetic limitations due to spin transitions, including surface reactions that result in the mobilization/immobilization of environmental contaminants. One such example would be the sorption and reduction of U(VI) as a uranyl cation, $(UO_2)^{2+}$, to form U(IV) species on pyrite. In this case, uranyl is low-spin but reacts to form U(IV) with each U having an $S = 2$ (uraninite, UO_2, is antiferromagnetic). A similar case is the reduction of chromate with Cr(IV) in solution to Cr(III) which typically forms the solid chromite. High-spin Fe minerals such as pyrrhotite[26] and magnetite[45] aid in this process.

Spin-transition barriers are known to variously affect reactions pathways. In biochemical systems, it is known that the formation of radicals is a result of the of the energy barrier imposed by spin selectivity rules.[42] Some organisms have found a way around these barriers, using oxygenase enzymes to activate $^3O_2$ and lower the activation energy for the spin transition via multiple electron and proton transfers and multiple diradical intermediates.[46] In surface catalysis, the abstraction mechanism or spin catalysis is a process by which oxidation by $^3O_2$ can occur without violating spin selection rules.[47, 48] For instance, the abstraction mechanism for an O_2 molecule involves O_2 approaching a surface end-on and the spin being shifted to the O that is further away from the surface. In this way, one O atom can adsorb in a singlet state, while the spin is efficiently carried away with the other O atom either being repelled back into the vacuum/aqueous solution or moved to a distant place at the surface where the spin can be accommodated (more on this later). This has been shown with $^3O_2$ adsorbing to Al(111) surfaces[49], arsenic sulfide clusters[23] and to UO_2 surfaces.[27] A second pathway to conserve spin angular momentum during a reaction is the transfer of spin to another site on the surface. Becker, et al. [22] demonstrated that spin density can be accommodated, and in effect, diluted on semiconducting surfaces by unpaired electrons residing at undercoordinated Fe at corner and kink sites, vacancies or by adatoms nearby on the surface. Additionally, the concept of spin being accommodated by an adatom on a surface is central to the field of spin catalysis.[50]

An additional complexity for semiconducting minerals like pyrite is that for many adsorption/desorption reactions taking place on the surface, the semiconducting properties of the surface introduce the possibility for unique behavior, such as the coupling of spatially

separated redox species by electron transfer (and electron spin transfer) through near surface layers. Thus, spin can be accommodated at sites remote to the initial reaction site. This indirect interaction is a type of "proximity effect" whereby the accommodation of spin density at one surface site modifies the reactivity of a remote surface site several Angstroms or even nanometers away.[22, 24]

From a computational modeling perspective, a poor accounting of the electronic spin state of the pyrite surface can lead to significant inaccuracies in ground state energy calculations. This will be especially important to accurately calculate minimum energy crossing points, or "saddle points", between the potential energy surfaces of different spin states.[42] Thus, it is appropriate to review what is currently known about the spin state of bulk and surface Fe in pyrite.

Pyrite is generally considered a diamagnetic (low-spin) solid with an experimentally determined band gap reported in the range 0.8 - 1.2 eV.[51, 52] The low-spin state is the result of the six-fold octahedral coordination of Fe by S as disulfide anions. In this arrangement, the CFSE is sufficiently large to restrict all six electrons to three t_{2g} orbitals (d_{xy}, d_{yz}, and d_{xz}) with each t_{2g} electron being paired so that Fe has a net spin of 0. Refinements of the diamagnetic interpretation of the bulk magnetic structure are posited by[53, 54] who describe that a trigonal distortion of the Fe octahedron in bulk pyrite results in an additional splitting of the t_{2g} orbitals into a_g and e_g orbitals. Indeed, non-negligible occupancy of the e_g orbitals indicates that pyrite is not a purely diamagnetic solid despite its bulk electronic properties.

Deviations from bulk-like properties also results from bond breaking associated with the formation of surface sites (terraces) or defect sites (step edges and corners) containing undercoordinated Fe as predicted by ligand field theory.[55] Generally, the CFSE of Fe decreases as its degree of coordination decreases, and if the energy gap is sufficiently small, electrons can jump from t_{2g} to e_g orbitals (d_{x2-y2} and d_{z2}) to form intermediate-to-high spin states. Thus, it is possible that undercoordinated Fe on the pyrite surface can accommodate spin density in contrast to the bulk. Experimentally, intermediate-to-high spin states have been identified on vacuum-fractured pyrite surfaces from the multiplet splitting of Fe(II) and Fe(III) peaks in X-ray photoelectron (XPS) spectra.[56, 57] Nesbitt, et al. [56] describe the multiplet splitting of the Fe 2p line as being due to stabilization of intermediate spin states for Fe(II) at terrace and step edges and high spin states at threefold coordinate sites at corners. Additionally, Nesbitt et al. suggests the formation of paramagnetic Fe(III) due to an auto-oxidation process that occurs at the surface, whereby the breaking of the disulfide (S-S) bond results in the formation of an S^- anion followed by an electron transfer from Fe(II) to the S^- to form Fe(III) and S^{2-}. As a result of this charge transfer, the resulting electrons on Fe end up being unpaired and produce electronic spin states on the surface.

Quantum-mechanical calculations of the spin state(s) of pyrite surfaces reveal many discrepancies between results from different studies. Studies suggest that spin polarized states are absent at the (100) surface.[20, 58] However, other studies indicate significant spin density located at Fe in stoichiometric and S-deficient (100) surfaces.[59, 60] Calculations by[61] predict that surface Fe in fourfold coordination, present on the (110) surfaces, are spin

polarized, while those of fivefold coordination are fully spin-paired. Alfonso [30] shows that various terminations of the (001) and (210) surfaces are spin neutral similar to the bulk material, while a (111) face terminated by three layers of S atoms is spin-polarized.

In view of these discrepancies, we set out to determine the degree of spin polarization at pyrite surfaces using the CFSE of Fe *d* orbitals located at specific surface sites. Although crystal field splitting energy values for bulk Fe have been reported for pyrite[55, 62-65], no such values have been determined for undercoordinated Fe at specific sites on the pyrite surface. We test if the extent of crystal field splitting governs the pairing of electrons within the non-degenerate *d* orbitals and that CFSE could be used to predict the degree of spin polarization of Fe (from Mulliken or Bader unpaired electron spin-densities) at specific surface sites. The electronic spin state and CFSE of Fe in pyrite is investigated by quantum-mechanical DFT using molecular clusters of various compositions and periodic surface models.

2 Computational details

In this study, we employ the widely-used hybrid HF-DFT B3LYP functional[66-68] for the energy evaluations of a series of neutral stoichiometric pyrite clusters of molecular formula, Fe_xS_{2x} (where x = 4, 8, 16, and 32; the cluster stoichiometries and their electronic structures for x=12, 18, and 24 were also calculated and analyzed but omitted in this manuscript for clarity). We investigate the energy, spin distribution, and crystal field splitting in Fe atoms of pyrite clusters as a function of allowed overall spin multiplicities. For Fe, the LANL2DZ basis set and its corresponding pseudopotential was used. For S, the LANL2DZdp basis set (which includes polarization functions) and the LANL2DZ pseudopotential were employed. This type of pseudopotential approach has been previously applied for the Fe(II) systems [69-72]. Thus, we employ the LAN2DZdp for the description of Fe atom. Geometries were not optimized in order to partially take into account the role of the underlying bulk; in addition, since hundreds of different cluster/spin configuration combinations were considered, the computational costs would have been prohibitively large. In addition, we are not interested in the energetics of crystal relaxation energies; rather we concentrate on the energy as a function of spin distribution and determine the crystal field splitting patterns for different Fe(II) ions and their local coordination environments such as the surface, edge, and corner sites that are present in pyrite cluster models. All cluster calculations in this work utilize the Gaussian 09 computational package.[73]

Our goal is to determine CFSE for bulk, surface, edge, and corner Fe(II) ions of pyrite and the energetics of different spin configurations for a given cluster size and geometry. In order to determine the CFSE of *d* orbitals of Fe(II) ions, natural bond orbitals (NBO) were obtained from DFT calculations.[74] NBO analysis provides the energy of each *d* orbital for every Fe(II) ion and from each energy difference between the t_{2g} and e_g set, the crystal field splitting energy is calculated.

In addition to systematic low-spin (LS) singlet to high-spin (HS) ferromagnetic (FM) state computations, antiferromagnetic (AFM) configurations were evaluated, for which the ”fragment” guess approach was employed as implemented in the Gaussian09 computational

package.[73] This approach can be used to guess and/or enforce individual specific spin states for particular atoms or atom groups as per our requirement; for example, an AFM singlet state can be generated by appropriately aligning the spin states of different atoms with opposite spin states.

Since most environmentally important redox reactions on pyrite occur under aqueous conditions and these alter CFSEs, we used the conductor-like polarizable continuum model (CPCM)[75-77] which treats the solvent as a dielectric continuum. This approach constructs a cavity around the cluster by imposing interlocking spheres around individual atoms, and the hydration energy stems from the interaction of the dielectric fluid with the cluster at the interface of the cavity. The dielectric constant applied is 78 which is ε_r for water. This dielectric continuum influences electrostatic interactions and dangling bonds that would otherwise extend into the vacuum. Although this approach can describe solvation effects to some extent, for a precise description of local hydrogen bonding effects, we used hydration models with explicit water molecules and determined the effect of water as a weak ligand on CFSEs.

Mulliken unpaired electron spin density value obtained for a specific atom represent the spin preference of that atom/ion. To choose either Mulliken spin density or Hirshfeld spin density for our further analysis, we applied both methods to the pyrite clusters such as Fe_4S_8 and Fe_8S_{16}. The results suggest that the absolute values of the Mulliken unpaired electron spins are minimally closer to formal spins of Fe(II) than the Hirshfeld spin density values (See ESI tables S7 and S8). However, the values using these two different methods differ by less than 0.05 unit charges, a difference that is irrelevant for interpreting the spin state of ferrous iron in pyrite as low, intermediate, or high. In addition, Bader charges and spins were used, which are based on the charge density distribution. First, a volume around each atom is determined by finding points between atoms where the electron flux perpendicular to that surface vanished (i.e., the dot product of a vector perpendicular to the determined surface around and atom and the electron density gradient, $\nabla\rho$, is zero). Along the connection between atoms, this is equivalent to the "bottlenecks", or saddle points of the electron density. Once the volume element for each atom is defined, charge ($\alpha+\beta$) and spin ($\alpha-\beta$) density are integrated over this volume around each respective atom to obtain atomic charge and spin. This approach obtains values atomic charge and spin that takes the electronic nature of the nature of the electronic nature of the bonds into account.[78-80]

For the solid-state calculations, we used DMol^3 and CASTEP modules of the Materials Studio package 7.0 [81, 82]. The generalized gradient approximation (GGA-PBE)[83] was used for solid-state calculations with periodic boundary conditions (bulk, 2D surfaces) as implemented in the DMol^3 program package.[84] The experimental crystal structure of pyrite is used for the geometry optimization of the periodic models. Convergence of the maximum atomic forces was set to a value of 0.11 eV/Å. Self-consistent field (SCF) energy accuracy was set to $2.7\cdot10^{-5}$ Ha (0.73 meV). Basis sets used were DND combined with DFT semi-core. A Monkhorst-pack[85] grid was used to create k-point integrations (separations of 0.04/Å). For the bulk geometry optimization, an energy tolerance of $2x10^{-5}$ Ha (0.54 meV) was used. An initial number of unpaired spins of four corresponding to the formal spin of

Fe(II) was set and then let to relax during the structural minimizations. A spin-unrestricted formalism was employed. The band structure was calculated in order to obtain the bandgap value of bulk pyrite and surfaces. The pyrite (100) surface was generated by cleaving the optimized bulk pyrite at the Miller planes (hkl) of (100) and keeping the disulfide groups intact. Then, a vacuum slab of 10 Å is introduced in the *c* direction. Subsequently, optimization was performed with the same criteria as used for the bulk optimization, but the cell parameters were not optimized to reflect the geometry constraints imposed by the underlying bulk.

The DMol^3 GGA-PBE 2D surface calculations using atom-centered basis functions result in a LS state for surface Fe(II) ions. In order to check this, we used the planewave-based CASTEP GGA-PBE approach with a cut-off energy value of 300 eV.[83] The Pulay density-mixing scheme was employed for spin mixing. The SCF energy tolerance was set to $1 \cdot 10^{-4}$ eV and the same tolerance was applied to geometry optimizations using a force tolerance of 0.05 eV/Å. In order to understand the electronic structure of pyrite bulk and 100 surface, band structure, density of states (DOS), and partial density of states (PDOS) were calculated.

3 Results and Discussion

First, we discuss the relative energies of pyrite cluster models as a function of total system multiplicity or spin state. The cluster compositions described here are chosen such that each larger cluster model contains one more type of surface site, *i.e.*, starting from corners only (Fe_4S_8), adding edge cations (Fe_8S_{16}), flat terrace sites ($Fe_{16}S_{32}$), and bulk-like Fe atoms ($Fe_{32}S_{64}$). Second, the CFSE of Fe ions corresponding to the most energetically favorable spin state are being discussed. Finally, we explain the results of periodic solid-state calculations of pyrite bulk and surface, for example, to evaluate if surface sites on a cluster show similar electronic structure as surface sites on an extended flat surface.

3.1 Cluster models

3.1.1 A small cluster with only corner Fe atoms: Fe_4S_8 cluster

The Fe_4S_8 cluster (shown in Fig. 1) is the smallest pyrite unit that can be modeled while preserving the pyrite stoichiometry and structure. The cluster is basically a cube (indicated by lines in Fig. 1) with four corners comprising Fe ions and the other four being disulfide anions. Due to the orientation of the disulfide groups in the four possible directions of body diagonals, this cluster assumes three-fold symmetry with the symmetry axis going through the disulfide group shown in the upper right corner in Fig. 1. As shown in Fig. 1, each Fe atom is a corner atom, coordinated to three sulfur atoms (in contrast to 6-fold coordination in the bulk). Therefore, the CFSE is expected to be less than in the bulk which allows for the possibility of spin polarized Fe. In order to test this hypothesis, the relative energies of pyrite clusters ($RE = E_{with\ spin} - E_{low\text{-}spin}$) as a function of multiplicity are shown in Fig. 2.

In the Fe_4S_8 cluster model, all four corner Fe ions are undercoordinated with the coordination environment consisting of three sulfide ligands in a mono-dentate orientation; however, there are two different sets of Fe atoms, the one on the lower left in Fig. 1 is on the

three-fold axis and the other three are off the axis and related by C_3 symmetry. In addition to the low-spin state (denoted as a reference point in Fig. 2, M = 1 and defined as E = 0) and all possible ferromagnetic intermediate- to high-spin states, two antiferromagnetic (AFM) spin configurations were examined. In the AFM singlet state, AFM(1), the spin states of Fe ions are arranged opposite to each other which cancels the overall spin and results in in an overall spin of zero (this spin state breaks the atomic symmetry of the cluster). In contrast, in the other AFM (SM=9) state, the Fe ion on the symmetry axis is assigned a high-spin down state and the remaining three as high-spin up states, which results in a net spin state of eight (note that AFM(9) would be antiferromagnetic when extrapolated to an infinite bulk, but due to the limited size of the cluster, there is no complete cancellation of spins and thus it could be considered ferrimagnetic).

All Fe ions in the Fe_4S_8 cluster are undercoordinated in a vacuum environment. However, in aqueous solution, dangling bonds on Fe can be satisfied by solvating water molecules. In order to understand the effect of solvation or hydration on the CFSE and REs, we first introduce the solvent effect using a dielectric continuum model and later a hydration model using explicit water molecules. The calculated REs of the Fe_4S_8 cluster in the vacuum and dielectric continuum as a function of various possible overall spin-configurations are shown in Fig. 2. High-spin (HS) and HS-AFM configurations are thermodynamically more favorable in both the vacuum and dielectric continuum than the low-spin states that one finds in the bulk. In fact, the dielectric phase further stabilizes the HS for multiplicities above 13 and HS-AFM states by another ~0.5-0.6 eV compared to the vacuum calculations. The results indicate that the AFM states are relatively more stable (i.e., lower in energy by ~0.4-0.45 eV than the lowest energy ferromagnetic spin configurations. Although we imposed C3 symmetry for the atomic arrangement of this cluster model, the resulting electron density matrix breaks the symmetry and adopts C1 symmetry; thus the C3 symmetry cannot be preserved for the molecular orbitals.

The *d*-orbital energies and calculated CFSEs for individual Fe ions are summarized in Tables 1-3. The splitting energies for the low-spin singlet state are spread over an energy range of 0.4-1.53 eV. When the low-spin singlet state (M = 1) is enforced for the cluster, the CFSE of Fe on the 3-fold axis shows a high CFSE of 1.53 eV, which is in excellent agreement with the experimental splitting energy of Fe ion in iron sulfide minerals (1.56 eV).[64] However, a closer look at the energy states of the Fe *d* orbitals shows that it does not strictly correspond to an O_h crystal field. The d_{z2} orbital energy is lowered, which is due to symmetry reduction (i.e., there is no ligand polarization for the d_{z2} orbital). Although the calculated CFSE agrees with the experimental value, it corresponds to the energy difference between the d_{x2-y2} and d_{z2} orbitals (see Schematic 1).

Our calculated relative energies as a function of multiplicity show that the HS cluster (M = 17) is the most energetically favorable ferromagnetic arrangement and the AFM arrangement is the most energetically favorable spin configuration overall. The relatively smaller CFSE values for undercoordinated Fe allows d electrons to occupy e_g orbitals and assume high spin states (see Table 2). Our results are consistent with ligand field calculations of pyrite that show Fe with a coordination number < 6 has a CFSE of 0.35 eV.[55]

The computed REs reveal that the AFM spin configuration is the most stable configuration. The undercoordination (lack of z-direction ligand coordination) lowers the energy of d_{z2} orbital and allows the electrons to occupy e_g orbitals which results in HS states. Our results are consistent with ligand field calculations of pyrite that show an Fe(II) with a coordination number < 6 has a CFSE of 0.35 eV.[55]

3.1.2 Effect of water on the crystal field splitting

In order to better understand the effect of hydration on the CFSE of Fe in the Fe_4S_8 cluster, we modelled the cluster hydrated with 12 explicit water molecules. Adding three water molecules per Fe ion restores the local octahedral (O_h) coordination (i.e., threefold coordination to water-O atoms and threefold coordination to pyrite-S atoms). Here, the HS-FM state (M = 17) and LS singlet state are calculated. The HS-FM state is more energetically stable than the LS state by 1.15 eV. This is about four times less than the vacuum case shown in Fig. 2. This is expected as the hydrating water molecules partially replace the missing sulfide ligands. However, water is not as strong of a ligand as sulfide and, thus, the ligand field strength of the Fe atoms is not fully restored. In addition, hydrogen bonds between water molecules tend to pull some of them out of their octahedral position (see below). This results in the HS case in an aqueous environment still being slightly more energetically favorable than the aqueous LS state. Using explicit water also shows that while the dielectric continuum model may be a fair representation of the hydration energy of atoms and molecules in many cases, it does *not* provide the field strength that would be representative of the ligand field energy of explicit water molecules.

The DFT-B3LYP optimized cluster models in Fig. 3 show an arrangement of water molecules consistent with undercoordinated Fe accommodating spin. For the HS-FM (M=17) case, the optimized geometry displays extended H-bonded water structures. Among the four Fe ions, two of them have a CN number of 5, and of the other two, one is 6- and the other one is 4-coordinated. In contrast, for the LS singlet optimized model, all the Fe ions show a local coordination number of six which is in accordance with the expected O_h LS crystal field.

For the FM-HS state, the calculated *CFSEs* are small which causes the electrons to occupy all available *d* orbitals. It is difficult to characterize the splitting pattern comprehensively, since further energy splitting within the t_{2g} and e_g sets is observed. However, the calculated splitting energies correspond to the energy difference between the fourth lowest orbital to the third lowest one (in analogy to having three low-lying t_{2g} and two higher e_g orbitals). In comparison to the LS singlet case, the addition of explicit hydration lowers the splitting energies significantly by 0.3-0.5 eV.

3.1.3 Fe_8S_{16} cluster

Increasing the cluster size includes edge sites in addition to the four corner sites. Thus, the Fe_8S_{16} cluster model contains two different Fe local coordination environments. The Fe atoms with CN = 3 correspond to corner sites and sites with CN = 4 to edge sites. Thus, Fe in this cluster is comprised of four corner and four edge sites (see Fig. 4). Figure 5 shows the relative energies of the cluster model as a function of different possible spin-multiplicities

(for this and larger cluster sizes, only in vacuo calculations were performed due to the number of spin configurations considered and the computational cost involved).

The calculated REs of the Fe_8S_{16} cluster as a function of multiplicity suggest that the FM state with all Fe in the high spin state is the most energetically favorable; however, AFM states are lower in energy than FM states by another ~1 eV similar to the Fe_4S_8 cluster. For the Fe_8S_{16} cluster, there are different ways in which the spins of the Fe can be arranged and four different AFM states are examined here for comparison. The RE difference between three of the examined AFM states are negligible. The exception is the AFM2 state, which corresponds to a specific spin arrangement, in which the left four Fe atoms (see Fig. 4) are assigned to HS-down, and the remaining four Fe on the right are assigned to HS-up. In this arrangement, up and down spins are not close enough to produce an effective AFM exchange. The other three AFM states correspond to an alternating arrangements of up and down spins (e.g., alternating up and down in every or every other Fe layer perpendicular to the (100) direction), which effectively cancels the overall magnetic moment. These results suggest that there are different spin configurations that will yield an AFM arrangement, but the energy differences between these states are negligible.

The calculated CFSEs for the HS-FM state are small due to undercoordination (0.5 eV and 0.6 eV for two Fe ions and about corner 0.01 eV for the other two), except for two of the four corner Fe, visible at the upper right and left corner of the cluster in Fig. 4, which are high – on the order of 1.5 eV; these Fe are labelled 3Fe and 8Fe in Table 4). The fact that the smaller CFSEs determined for the HS-FM state is due to the lowering of e_g orbitals which causes the splitting of the e_g set into $b_1(d_{x2-y2})$ and $a_1(d_{z2})$ and the t_{2g} set to $b_2(d_{xy})$ and $e(d_{xz}$ and $d_{yz})$ orbitals (see Schematic 1). The relatively small CFSE of the HS-FM configuration (M =33) is evidence that electron pairing energy is stabilizing the cluster. The electron pairing energy of Fe calculated using the HF method is reported in the literature[86] to be 2.4 eV. In the AFM configuration, all Fe ions are in a HS state with the spins opposite to each other providing a maximum additional stabilization of ~1.0 eV.

Specifying a LS singlet state requires all six electrons in the *d* orbitals of Fe ions to be paired, which allows for an O_h splitting pattern of d orbitals. The splitting pattern of the Fe ions of the LS singlet state are similar to what is expected for nondegenerate *d*-orbitals in O_h coordination. An O_h splitting pattern is noted for half of the Fe ions (two corners and two edges). Furthermore, examining the calculated CFSEs of the Fe ions of the LS singlet state reveals that the calculated CFSE and the pattern of *d*-orbital splitting are consistent with an O_h crystal field. The key point here is that the calculated CSFE values 1.49 and 1.51 eV for the two corner 3Fe and 8Fe, respectively, are in agreement with the reported experimental value of 1.57 eV. In addition to the CFSE (see Schematic 1), there is another splitting within the t_{2g} set of orbitals. The d_{yz} orbital is stabilized by 0.4 eV relative to the d_{xy} and d_{xz} orbitals and the e_g set of orbitals show a splitting energy difference of 0.2 eV. The other two Fe ions also show an O_h splitting pattern with a calculated CFSE value of ~0.8 eV. For these Fe atoms, there is an additional splitting within the e_g set of orbitals (d_{z2} and d_{x2-y2}) and the splitting energy value is ~0.7 eV which is in excellent agreement with the proposed splitting

value of ~0.60 eV by Schlegel and Wachter [65] If these two values are added together, the resulting CFSE value of ~1.5 eV matches well with the experimental value. For the remaining four Fe ions, the d_{z2} orbital is stabilized which causes the energy of this orbital to drop below the t_{2g} orbital. This is a clue that the t_{2g} orbital set is splitting within the set. The CFSE values calculated for these Fe ions are within the range of 0.1-0.4 eV.

3.1.4 $Fe_{16}S_{32}$ cluster

This cluster model contains four corner, eight edge, and four surface Fe sites (CN = 5). The calculated REs with respect to the permissible spin multiplicities are fitted to a third order polynomial which is shown in Fig. 6, and shows that multiplicities of 41, 45, 49, 53, and 57 have similar REs with respect to the LS singlet state due to similar distributions of HS, IS, and LS states of different Fe atoms in different positions. Multiplicities higher than 57 (that do not allow for sufficient LS and IS states) show an increase in energy.

In order to determine the AFM states of the $Fe_{16}S_{32}$ cluster and its relative stability with respect to the most stable spin states, we consider two different AFM states. In one case, we assign a HS for surface Fe atoms and in the other case we assign an IS for surface Fe(II) atoms. The results suggest that the AFM state significantly stabilizes the pyrite cluster by about ~0.97 (HS-AFM) and 1.44 eV (IS-AFM) Although we assigned HS states for all four surface Fe(II) ions in the HS-AFM state, two of the surface Fe(II) atoms do not retain the HS state rather they show IS states at the end of the completed SCF cycles and in the IS-AFM (surface Fe(II) are treated IS states) retains the specified IS states for all the four surface Fe(II) atoms. The calculations show that for AFM configurations, the stabilization due to the AFM coupling is significantly more than the energy difference between the HS and IS states of the surface Fe(II) atoms. In summary, AFM coupling is the most favorable ordering scheme and favors HS or IS states for surface Fe(II) atoms with little energetic difference between them.

Small CFSE values of some corner and edge Fe(II) ions in this cluster agree with the values for the calculated HS state in the smaller clusters. The surface Fe(II) atoms (that did not exist in smaller clusters) favor the intermediate spin state (Table 5). Forcing the system to the LS singlet state increases the calculated CFSE values significantly and the determined CFSEs of the LS singlet state are within the range of ~0.7-1.4 eV. For the SM=53 configuration, in addition to the four surface Fe(II) atoms, two of the edge Fe(II) ions show an IS spin state. In the SM=57 configuration, all the surface Fe(II) atoms show an IS spin state. Another noteworthy point is that the disulfide ligands share a significant amount of unpaired electron spin densities, which demonstrates that the Fe-S coordination bonds are not purely ionic but rather with a certain amount of covalent character.

3.1.5 $Fe_{32}S_{64}$ cluster

In the sequence of cluster models discussed in this manuscript, this is the first one to introduce bulk Fe ions. There are four bulk-like Fe atoms in the $Fe_{32}S_{64}$ cluster with O_h coordination by sulfide. In addition to these four bulk-like Fe ions, the remaining 28 Fe are comprised of 4 corner, 12 edge, and 12 surface Fe atoms. This $Fe_{32}S_{64}$ cluster has C3 symmetry (see Fig. 8) with a three-fold axis going through the body diagonal of the cluster

cube, similar to the Fe_4S_8 cluster (note that, in contrast to the NaCl structure, the finite size of the cluster and the existence of disulfide groups reduces the symmetry such that this three-fold axis has to go through the Fe atom on the lower left bottom in the cluster in Fig. 8 and the upper right disulfide group; in the rocksalt structure, we would have four equivalent body diagonals instead of just one).

The coordination of corner Fe(II) atoms with S atoms is approximately pyramidal, in which the S-Fe-S angle is 94.3 ˚ for all three S ligands; thus the corner Fe atoms attain a local C_{3v} symmetry. Edge Fe atoms display a distorted tetrahedral (T_d) bonding environment with an approximate D_{2d} symmetry. Surface Fe atoms acquire a local square pyramidal (C_{4v}) symmetry. Thus, if a bulk Fe becomes a surface Fe, it loses one of the S ligands and adopts a square pyramidal geometry. Further, if a surface Fe atom becomes an edge Fe, it loses another S ligand and resulting in a distorted tetrahedral (D_{2d}) geometry. In the transition to a corner Fe, the loss of another S ligand results in a symmetry reduction to C_{3v} and the splitting pattern of this point group is similar to the T_d point group.

We next consider the splitting pattern of these various Fe sites in the cluster. For the bulk Fe, the splitting of the degenerate *d* orbitals results in a set of t_{2g} and e_g, as expected for an O_h symmetry. In this setup, the lowest energy t_{2g} orbitals are completely filled and the low-spin configuration is energetically favored. In contrast, for the surface Fe, as a consequence of the symmetry reduction, not only the degeneracy of t_{2g} orbitals is perturbed, but also the loss of one the S ligands lowers the energy of the d_{z2} orbital. The outcome of this reflects the symmetry of the orbitals as well as their relative energies. A small energy difference between the b_2 (d_{xy}) and a_1 (d_{z2}) orbitals allows the paired electrons in the b_2 orbital to occupy the a_1 orbital to produce a high-spin configuration. For a complete schematic of *d*-orbital splitting pattern under various Fe local coordination environments, see Schematic 1.

Due to the cluster size (which would generate a huge number of possible spin configurations with each configuration/run coming at a high computational cost), we did not do an extensive RE analysis as a function of allowed spin configurations, based on the experience with smaller clusters, we calculated two AFM states. One of the AFM states refers to an overall spin multiplicity of 9, which is a result of the combined positive (up) spins of 15 Fe(II) ions and negative (down) spins of 13 Fe(II) ions. These 28 Fe(II) atoms represent undercoordinated Fe(II) atoms and the remaining four Fe(II) are treated as lows spins in order to mimic the diamagnetic LS state of pyrite bulk Fe(II). As this $Fe_{32}S_{64}$ crystal shows C_3 symmetry (see Fig. 8), we imposed alternating up and down spin states perpendicular of the three-fold axis in the [111] direction. Whilst giving HS state for the surface Fe(II) atoms results in a ferrimagnetic state of spin multiplicity, 9. In contrast, the surface Fe(II) ions equally prefer an intermediate spin (2 unpaired electrons), when we assign this IS to the surface Fe(II) ions results in a FM state of spin multiplicity, 5.

The unpaired Mulliken spin density values show that all Fe atoms, except for two of the terrace Fe(II) ions, retain the initially specified spin value of 4. For the bulk Fe ions, the calculated Mulliken spin density values are ~0.3-0.4 (Bader spins are ~0.0-0.03) (Fig. 8), which is an indication that these Fe(II) ions are low-spin and diamagnetic. However, the

surface (terrace), edge, and corner Fe(II) ions show spin density values of ~3.3-3.5, which corresponds to a HS state. Only two surface Fe(II) ions show an intermediate spin of ~2, which is not surprising because this can be expected and in fact this intermediate spin state for surface Fe(II) has already been documented in the literature by DFT [59] and predicted by classical ligand field theory.[55] In addition, this observation is in line with our aforementioned results on the favorability of IS states of surface Fe(II) ions.

Obtaining an intermediate spin value of ~2 for two of the terrace Fe(II) ions motivated the investigation of intermediate spins states for surface Fe(II) atoms. Hence, in another AFM state calculation, intermediate spin states were specified for all surface Fe(II) atoms, while the bulk Fe(II) ions were kept as LS states, and evaluated the RE difference between the two calculations. The assignment of intermediate spin states for all surface Fe(II) atoms results in an overall SM of 5. In order to understand the stability of IS against the HS state of the surface Fe(II) ions, we examined these two different spin states. As a result of spin up and down configurations, the resulting net spin state of IS-AFM and HS-AFM are 4 and 8, respectively. Remarkably, the calculated RE difference between the two AFM states show that the IS-AFM state is ~3 eV more stable than the HS-AFM. This larger cluster shows the preference for IS surface Fe atoms in a more pronounced way than the smaller clusters. Thus another factor that controls the spin states of the cluster models is the size of the employed cluster; overall, the cluster size has to be taken into account when considering the spin states of nano-clusters because, to some extent, the cluster size switches the spin state preference of surface Fe(II) ions. The IS-AFM model preserves the specified spins for the Fe(II) ions and no unusual spin change of Fe(II) spin is noted. Significant unpaired electron spin distribution on S-atoms is noted (~0.2-0.5). This causes the reduction of actual unpaired electron spin-density values on Fe(II) atoms, further indicating that the Fe-S bond is not purely ionic but with some covalent character.

In order to examine the relative stability of the AFM states (HS-AFM and IS-AFM) with respect to the LS singlet state, the LS singlet state is calculated for this cluster model. Based on our experience with the calculation of REs of pyrite clusters as a function spin states, the lowest energy states are expected to be about ~7-8.5 eV more stable than the LS singlet state. In fact, our calculated RE difference between the LS and HS-AFM and IS-AFM states are 7.64 and 10.65 eV, respectively.

The determined CFSEs of various Fe(II) ions in the $Fe_{32}S_{64}$ cluster and the corresponding *d*-orbitals are summarized in Table 6. For the HS-AFM state, the bulk Fe(II) atoms show CFSEs in the range of 0.3-0.9 eV. In contrast, in the IS-AFM state, for two of the Fe(II) ions, the CFSE values obtained are smaller and are within the range of 0.1–0.8 eV. Although these bulk Fe(II) ions show different CFSE values for the investigated AFM states, the calculated Mulliken spin density values (~0.35) indicate that these are indeed LS states. The calculated CFSEs for the corner Fe(II) ions are ~0.2 eV for the HS-AFM state, whereas for the IS-AFM state, two of the Fe(II) ions agree with the HS-AFM state values, yet two of the Fe(II) ions show about ~0.6 eV higher CFSE values than the HS-AFM state CFSE values. However, the calculated Mulliken unpaired electron spin density values (~3.3) indicate that these corner

Fe(II) ions prefer a HS state while the edge Fe(II) ions are in HS state Fe(II)s (spin densities of 3.2-3.4, CFSEs in the range of 0.2-0.3 eV). In general, the calculated smaller CFSE values are in excellent agreement with the computed Mulliken spin densities and demonstrate that the edge Fe(II) ions favor HS states. For the IS-AFM state, the calculated CFSEs for most of the edge Fe(II) ions show a range of about 0.1-0.5 eV, and this wider range may be due to the specified overall spin multiplicity value

Despite the initial assignment of HS states to all Fe atoms, two of the surface Fe(II) ions do not conserve the state and fall into an IS state. The calculated CFSEs of the surface Fe(II) ions show a range of 0.1-0.75 eV, depending on the range of the surrounding disulfide groups. The calculated Mulliken unpaired electron spin density values illustrate that the surface Fe(II) ions within the HS-AFM state mostly prefer the HS state; however, two of the Fe(II) ions show intermediate spin states.

In the IS-AFM state, the computed Mulliken unpaired electron spin density values indicate that all surface Fe(II) atoms are in an IS state. However, a range of different CFSE values is obtained for these Fe(II) ions. Three of the surface Fe(II) ions show CFSE values of about 0.7-0.8 eV and two Fe(II) show relatively large CFSE values of about 1.3 and 1.6 eV. Although the last value agrees with the experimental CFSE value of Fe(II) ions pyrite bulk, a close examination of the *d*-orbital splitting does not match with an ideal O_h splitting pattern, rather, internal splittings within the orbital (t_{2g} and e_g) sets are observed that cause the reordering of energy levels orbitals.

While the aforementioned CFSE values are describing the d-orbital level splitting of individual Fe atoms in specific surface positions and coordination, here we are putting these local electronic values in the context of experimental and computational band gap values of extended periodic structures. Previous experiments and computations have identified a range of bandgap values for pyrite surfaces from 0.16-0.72 eV. For moderate to large cluster sizes, the contribution of corner atoms is more or less negligible (there are only four of such Fe atoms for a perfect nano-cluster). For instance, in the $Fe_{32}S_{64}$ cluster, the states of surface and edge atoms are the main contributors to the bandgap reduction from the bulk value of 0.95 eV to the reported smaller values. The range of reported values indicates that it is difficult to isolate the individual contribution. However, one can assume that the bulk-like Fe(II) atoms likely increase the bandgap value because of their diamagnetic low-spin state. In contrast, the surface and edge atoms tend to decrease the bandgap value because the undercoordination of surface Fe(II) atoms increases the probability of a HS state.

There are a few points to consider when further discussing CFSEs. According to Burns [64], the CFSE reported for Fe ion in sulfides is 1.56 eV; at the same time, Schlegel and Wachter [65] reported a value of 1.7 eV for the transition from t_{2g} to e_g orbitals. For bulk pyrite Fe ions, based on CFT, this value has been determined to be 2 or 2.2 eV.[55, 62, 63] In addition, Schlegel and Wachter [65] reported an additional splitting of e_g set into two states and the splitting energy is ~0.6 eV ($d_{z2} - d_{x2-y2}$). Similarly, Bronold et al. proposed that the energy difference between the $d_{z2}(a_1) - d_{xy}(b_2)$ orbitals is 0.35 eV. If the electron pairing energy (Hund's rule, the tendency of electrons in a partially occupied shell to occupy different

orbitals, is based on electron repulsion in the same orbital which drive the energy up by the electron pairing energy) is less than this value, a low-spin state is possible; in contrast, if the electron pairing energy is greater than 0.35 eV, Fe atoms tend to acquire an intermediate spin. Bronold et al. proposed a high-spin state for this case based on a point-charge model, but our quantum-mechanical calculations show an intermediate spin state is more energetically favorable. In order for a high-spin state to occur, the energy of the b_1 orbital (d_{x2-y2}) has to drop by a certain amount to reduce the CFSE to an amount that is lower than the electron-pairing energy. This suggests that the energy difference between the $b_1(d_{x2-y2})$ and $a_1(d_{z2})$ orbital sets and between the $b_2(d_{xy})$ (or d_{yz}) and the set of degenerate d_{xz} and d_{yz} orbitals (or the set of d_{xy} and d_{xz} depending on the Fe considered) are small.

3.1.6 Crystal field splitting energies of $[FeS_6]^{-10}$, $[FeS_5]^{-8}$, $[FeS_4]^{-6}$, and $[FeS_3]^{-4}$ pyrite fragments

Crystal field splitting energies of various Fe(II) ions present in pyrite cluster models were discussed in earlier sections. In order to develop an understanding of the CFSE as a function of just the local Fe coordination environment, this section discusses CFSEs of Fe(II) ions of isolated pyrite fragments such as $[FeS_6]^{-10}$ (bulk-like), $[FeS_5]^{-8}$ (surface/terrace-like), $[FeS_4]^{-6}$ (edge-like), and $[FeS_3]^{-4}$ (corner/kink-site like) (for the structures, see SI, Fig.S2). These fragments are extracted from a bulk pyrite crystal, and energy calculations followed by NBO calculations allow determining *d*-orbital splitting energies. The determined CFSEs are compared with the cluster models in order to understand if the crystal field energy is mainly a result from the immediate coordination environment or if second and further nearest neighbors have a significant influence on the CFSE and spin state of Fe atoms in specific locations. All fragment energies are calculated in HS, LS, and IS configurations in order to determine which one is the most energetically favorable. REs are calculated with respect to the LS state. The Fe-S bond distances are exactly the same for all the six Fe-S bonds and the S-Fe-S angles would be 90˚ in an ideal octahedron but slightly deviate in the pyrite structure by about 4-5˚. The calculated REs of the pyrite molecular fragments with respect to the corresponding LS state are summarized in Table 7.

For the FeS_6 fragment, the LS state is ~0.5 eV more stable than the HS state. When considering the FeS_5 fragment, the RE difference between the LS and HS state is about ~0.05 eV, which lies within the error of the applied DFT approach, hence, either a HS or LS state is possible rather than an IS one, which is about ~0.23 eV less stable. The FeS_4 fragment represents an edge site and Fe(II) of this fragment favors HS state over LS and IS states. Subsequent removal of S-atoms from the coordination sphere of Fe(II) ion favors a HS state. Overall, the FeS_6 (bulk-like) fragment prefers a LS state and the FeS_5 (surface-like) fragment likely to exhibit either a LS or HS state. In contrast, the further symmetry reduced fragments such as the FeS_4 (edge) and FeS_3 (corner) prefer a HS state. In addition to the HS state, the FeS_3 also prefers an IS state, yet the probability is less.

The CFSEs calculated for the pyrite, FeS_n fragments are summarized in Table 8. The calculated CFSEs for the FeS_6 fragment corresponding to various possible spin states are in the range of 0.02-0.41 eV. Due to the tetragonal distortion of O_h geometry, further splitting within the t_{2g} and e_g orbital sets produces different energy orderings for resulting orbitals.

For instance, for the CFSE of 0.21 eV, the orbital energy levels show internal splitting in the e_g orbitals by 0.48 eV (d_{z2}-d_{x2-y2}) and in the t_{2g} set by 0.96 eV (d_{yz}–d_{xz}) (the corresponding *d*-orbital transitions are provided in parentheses).

For the FeS_5 fragment, the CFSEs calculated are in the range of 0.14-0.64 eV. The d_{xz} and d_{yz} are almost degenerate (lowest level), and the next ones up are the d_{z2} and d_{x2-y2}; the splitting energy difference between these two sets is ~0.5 eV. The d_{xy} orbital is the highest energy level, which is 1.38 eV higher than its degenerate lower level set of d_{z2} and d_{x2-y2} orbitals. For the FeS_4 edge-like fragment the CFSEs of various spin states are in the range of 0.1-0.3 eV. In the corner-like FeS_3 fragment, the calculated CFSEs are observed to be about 0.13-0.28 eV. There is no clear trend noted for the observed CFSEs whilst moving from the bulk-like FeS_6 to the corner-like FeS_3 which is an indication that the electronic structure is complex.

3.2 Periodic solid-state DFT calculations on bulk and surface pyrite

This section addresses the bulk and surface electronic structure of pyrite obtained from periodic solid-state DFT calculations with periodic boundary conditions. This is done to compare the electronic structure of the periodic bulk or surface slab with a bulk, terrace, edge, or Fe atoms in a finite cluster. First, we discuss the structural parameters obtained for bulk pyrite, the vacuum-terminated (100) surface, and the (100) surface with added water from our computations and compare the results with available experimental values. This is followed by bandgap values, ground state properties, and projected densities of states of specific Fe(II) ions, for instance, of bulk and surface Fe(II) ions and determine CFSEs of these Fe(II) ions from the PDOS peak positions.

3.2.1 Bulk pyrite

The GGA-PBE calculated lattice constant values (a=5.47 Å for DMol^3 and 5.40 Å for CASTEP, Table 9) are in remarkable agreement with the experimental value of a=5.43 Å. While the DMOl^3 calculation (based on atom-centered basis functions) predicts a small volume increase, the planewave approach CASTEP predicts a small volume decrease in comparison to experiment. Despite not using a Hubbard U-parameter for Fe(II), the calculated diamagnetic ground state of pyrite is accurately reproduced which is in accordance with experimental characterizations. The calculated geometrical parameters are presented in Table 9 along with previous computational and experimental results. Our calculated S-S and Fe-S bond distances and lattice constant values are in good agreement with the experiments within about ~0.02 Å. This gives confidence that the DFT method used here is capable of predicting accurate structural and electronic properties of pyrite and validates the employed approach.

GGA-PBE calculations using DMol^3 with atom-centered basis functions predicts a bandgap value of bulk pyrite of 0.95 eV, which is in agreement (within a few meVs) with the available experimental photoconductivity measurement[51, 52] value of 0.95 eV and agrees with previously reported DFT calculated values. In contrast, PBE calculations using the planewave approach implemented in CASTEP predict a bandgap value of 0.58 eV, which is lower than the experimental value; however, this value agrees with a previous computational

study.[58, 87] Although the computed bulk bandgap values are different from each other, the Fe(II) ion in bulk pyrite is predicted to be low-spin, which is confirmed from the calculated Mulliken unpaired electron spin densities.

The focus of this study is not in the predicted band structure or bandgap values, but the *d*-orbital splitting value of Fe(II) ion in bulk pyrite. From the projected density of states (PDOS) of the d-orbitals of Fe(II) ions of the optimized bulk pyrite, the d-orbital CFSE is determined. Two representative peaks corresponding to t_{2g} and e_g set of orbitals are shown in the PDOS (Fig. 9). The difference between the peak values gives the CFSE of the bulk Fe(II) ion of pyrite. The CFSE as determined in Fig. 9 (using the difference in energy between the maxima of the t_{2g} and e_g levels) we obtain a CFSE of 2.05 eV; if we consider the sub-splitting of the t_{2g} and e_g levels, this value would decrease. This is a possible explanation of the discrepancy between the experimental values by Burns et al (~1.56 eV)[64] and 2-2.2 eV by Stevens, et al. [53], Antonov, et al. [88], and[55, 62, 63]. The CFSE predicted using DMol^3 is ~0.25 eV (for the PDOS see SI, Fig. S1) higher than the CASTEP value. However, a general agreement is obtained between the predicted values.

3.2.2 Pyrite (100) surfaces

Calculated bandgap values for pyrite(100) and pyrite(100) surface with added water molecules are collated in Table 10. Contrasting results are obtained for the pyrite(100) surface calculations using the DMol^3 and CASTEP codes. The GGA-PBE CASTEP calculation predicts a metallic ground state, whereas the DMol^3 predicts a bandgap value of 1.16 eV, confirming a semiconducting ground-state for the pyrite (100) surface, which is ~0.1 eV higher than the bulk bandgap. There are several factors, which can be attributed to these distinct results; for instance, the CASTEP is a planewave code while DMol^3 uses Gaussian-like basis sets of atom-centered orbitals. In addition, the pseudopotentials are different, the DMol^3 uses DFT-semicore pseudopotentials, and the CASTEP code uses ultrasoft pseudopotentials in which the Fe-atom contains eight valence electrons and the S-atom contains six valence electrons and the remaining electrons are encompassed into pseudopotentials for both the atoms.

Whatever the initial formal spin assignment for *surface* Fe(II) ions in the DMol^3 surface calculations is, they end up in a LS state. In contrast, the CASTEP runs allow determining the possible HS and IS states for surface Fe(II) atoms. Unless the HS state is fixed, the assigned HS configurations for Fe atoms convert into IS states. Mulliken unpaired electron spin densities of ~2 obtained for surface Fe(II) ions of the pyrite (100) surface suggest that the surface Fe(II) ions prefer intermediate spin states. Arranging spins to an overall AFM singlet state results in a LS state for surface Fe(II) ions.

In contrast to a previous CASTEP study (GGA) of pyrite(100) surface which showed a small band gap of 0.16 eV[89] the current CASTEP study produces a metallic state for the pyrite(100) surface, which may be due to the use of planewaves in describing the molecular character of disulfides. Crossings between the valence and conduction band is an indication that the (100) surface behaves like a conductor. However, arranging Fe(II) ion spin states in

an antiferromagnetic configuration results in a bandgap value of about 0.54 eV, which is similar to the bulk bandgap value predicted by the PBE-CASTEP method.

3.2.3 Pyrite (100) surface with water

In order to test the hypothesis that adsorbed water molecules have a significant impact on the local electronic and overall band structures and spin states of surface Fe(II) ions, we added explicit water molecules to pyrite (100) surfaces and relaxed the models to reach their equilibrium geometry. Two cases were investigated: in the first one, we inserted a water molecule to one of the surface Fe(II) atoms. In the second case, we introduced water molecules to all surface Fe(II) atoms. For the single water adsorption case, the analysis of the calculated unpaired electron spin densities of surface Fe(II) atoms reveals that the water adsorption alters the spin of Fe(II) ions from high-spin to low-spin, which is not surprising and is expected because the adsorbed water molecule acts as the sixth ligand and fulfills the requirement of a classical O_h coordination. However, one can argue that water is a weak ligand in comparison to the anionic sulfide ligands, but the fact that fulfilling the vacant coordination of surface Fe(II) ions is adequate, to certain extent, to restore the crystal field significantly to a bulk-like environment, and further transforms the HS or IS state of surface Fe(II) atoms into a LS state. Consequently, this HS or IS to LS transformation of surface Fe(II) atoms modifies the conducting state of the surface into a semiconducting state with a well resolved bandgap value of 0.59 eV. Arranging the spin states of Fe(II) ions to an AFM state increases the band gap value by ~0.3 eV. However, adding water molecules to all surface Fe(II) atoms further increases the bandgap value by ~0.4 eV. These bandgap values suggest that a transformation from a conducting state to semiconducting state occurs when water adsorption takes place. In addition, the occurrence of the AFM state has a significant influence on the computed bandgaps and band structures. The DMol3-computed band gap values of different pyrite surfaces reveal no conducting state for the pyrite[90] surface. Also, arranging the spins states of Fe(II) ions to AFM state does not affect the band gap significantly and the semiconducting state is retained. However, the band gap values of surfaces are ~0.2-0.3 eV higher than the bulk band gap. Furthermore, addition of one water molecule to one of the surface Fe(II) atoms and assigning AFM states for Fe(II) ions have only a minor increase of band gap by ~0.1 eV. In contrast, addition of water molecules to all surface Fe(II) ions results in a band gap value of 1.68 eV which is ~0.8 eV higher than the bulk band gap. In summary, when the reactivity of surfaces is discussed, for example as a function of adsorbing ligands, hydration and corresponding changes of spin arrangements (e.g., AFM states) have to be taken into account. While this study focuses on the spin state of surface Fe atoms in the vacuum or gas phase, though indicating the effect of partially restoring the ligand field due to hydration, it would be very important to study the spin state extensively in an aqueous environment. Not only would pure water have an effect on the ligand field but also other ions (especially anions), *e.g.*, from background electrolytes that may be stronger ligands than water molecules.

In order to quantify CFSEs of surface Fe(II) atoms, we consider a bare surface Fe(II) ion and an Fe(II) ion bound to a water molecule. The PDOS for the bare surface Fe(II) and Fe(II)-W are obtained for the pyrite(100) surface with a single added water molecule are shown in Fig.

10. The PDOS illustrates that there is internal splitting within the t_{2g} and e_g set of orbitals. Comparing the bulk and surface Fe(II) ion PDOS profiles suggests that for the surface Fe(II) and surface Fe(II)-W ions, a new PDOS peak arises around the Fermi level at ~1.1 eV from the lowest energy t_{2g} set. This new feature observed for both the surface Fe(II) and Fe(II)-W indicates that water adsorption does not only alter the electronic state of Fe(II) where it is bound to, but also the immediate neighboring Fe(II) ions as well. Although new surface features are noted for the surface Fe(II) ions, the CFSE energy here is ~1 eV, which is by about ~1.1 eV smaller than the bulk Fe(II) ions.

4 Conclusions

This study investigates *d*-orbital splitting patterns of different coordination environments of Fe(II) atoms possible for a for a nano-pyrite particulate and pyrite surfaces by employing a range of clusters (Fe_xS_{2x}, where x = 4, 8, 16, or 32) and periodic solid-state (3D-bulk and 2D (100) surfaces) models. In addition, the REs of cluster models as a function of spin multiplicities are determined and spin states of surface Fe(II) atoms are determined. As the number of Fe-atoms increases in the employed cluster model, the coordination by S ligands increases from three to higher numbers up to a maximum of six for an ideal bulk-like octahedral coordination. For the bigger cluster models, FM states show unfavorable relative energies, which is due to the introduction of surface (terrace), and bulk-like Fe(II) atoms that do not prefer a LS state. Intermediate multiplicities for FM ordering are stable with a balance between HS, IS, and LS states. In addition, surface Fe(II) ions prefer a HS over an IS state in smaller clusters; in contrast, in bigger clusters, no such preference is observed. Furthermore, AFM ordering provides additional cluster stability due to exchange interaction and cancellation of net magnetic moments.

The energy of a pyrite cluster changes by more than a ~1 eV (*i.e.*, more than 100 kJ/mol) per Fe atom, depending on the local spin configuration, and, thus, the reaction energies of a redox reaction change by a huge amount as a result of considering unpaired spins. One difficulty in applying this concept is that textbook knowledge on t_{2g} and e_g states and splitting cannot be strictly applied, if the coordination environment is perturbed due to missing ligands and distortion of the local geometry; another one is that the spin state and orientation can be further influenced by reactants in the vicinity of the Fe atom at a mineral-water interface. While the first issue is dealt with in detail in this study, the second will be discussed in an upcoming one

Calculated CFSEs of different Fe(II) ion coordination environments such as corner, edge, surface, and bulk-like suggest that the undercoordinated Fe(II) ions show smaller CFSE values than the bulk-like Fe(II) ions. For instance, the undercoordinated Fe(II) ions show CFSE values of ~0.1-1.3 eV. However, often, the bulk-like Fe(II) ions also show smaller CFSEs, which is due to a trigonal distortion. A range of different CFSEs determined for various Fe(II) ions (bulk, terrace, edge, and corner) of the employed pyrite cluster model explain the complexity of bonding involved in pyrite, in particular nano-particulate pyrite. A

considerable extent of covalent character in Fe-S bond is expected which is confirmed from the observed unpaired electron spin densities of sulfide ligands.

Solid-state periodic boundary DFT calculations of bulk-pyrite and (100) surfaces are in accordance with previous computational and experimental findings. In particular, this study precisely reproduced the bandgap value of bulk-pyrite to be 0.95 eV. The results obtained for the pyrite(100) surface show a conducting ground state and arranging spins to an AFM state eliminates the conducting state and results in a semi-conducting state. In addition, addition of water molecules to the pyrite(100) transforms the conducting state into a semi-conducting state. For Fe(II) ion of bulk-pyrite, using periodic boundary solid state calculation, the CFSE is calculated from a PDOS profile and the value is about ~2.05-2.3 eV, which is in excellent agreement with the reported CFSE of Fe(II) ion (2-2.2 eV) based on CFT previously reported [55, 62, 63]. For the (100) surface, a CFSE value of ~1 eV is determined.

Ferromagnetic/AFM behavior of synthetic nano-pyrite clusters have been reported recently [91]. This explains that pyrite nano-clusters are expected to exhibit interesting magnetic properties. Our computed stable FM states for the smaller clusters and AFM states for the bigger nm sized cluster illustrate and confirm the hypothesis that the nano-clusters are different from bulk which can be used for tailored catalytic applications, for instance, reduction or electron transfer process. Furthermore, interesting optoelectronic properties, for example reduced bandgap for these nano-clusters are anticipated.

The fact that even for the same number of local ligands within the first coordination sphere of the metal atoms, the way in which the ligands arrange themselves controls the spin states of the metal ion and essentially contribute to the reactivity. This is helpful because if we can effectively arrange the surface atoms in such a way or create specific Fe(II) local coordination environments on a pyrite surface by creating S-atom vacancies, the surface reactivity of pyrite can be fine-tuned towards tailored applications. For instance, producing specific surface configurations will result in a promising reduced bandgap that can be utilized for solar-cell applications or electron transfer processes followed by reductive precipitation of contaminants.

The DFT approach is based on a single-reference system. As demonstrated in our earlier numerous spin configurations of cluster models, a number of unpaired electrons are possible for FM states. Considering this scenario makes us to think that a multi-reference and spin orbit interaction, although these are usually ignored for the first row TM complexes, can significantly influence the calculated CFSEs and ground state property of pyrite clusters. At the same time, employing a high-level ab initio method that treats spin-orbit interaction and multi-reference state are computationally currently too expensive for a cluster of *nm* size.

In a broader geochemical context, iron sulfides (probably most importantly pyrite and mackinawite) and iron (hydr-)oxides (hematite, goethite, and ferrihydrite) are among the most important natural phases to control the kinetics of redox reactions in natural environments and in anthropogenically influenced settings such as the reduction of actinides in groundwater. In some of these reactions, the sulfides act as the actual reductant, in others,

they are merely 'helping' in transferring electrons or dehydrating the reactants before electron transfer, thus catalyzing the reactions. However, in both cases, the existence of high-spin states on the surface greatly enhances the kinetics of the redox process because previously forbidden spin transition become spin-allowed as the Fe spin system can accommodate for the change in spin. This is the reason for why the kinetics of redox reactions involving pyrite assume an intermediate place between pyrrhotite (fast, all Fe atoms, including bulk-like ones, are in a high-spin state) and galena (slow, no unpaired spins). Thus, as evolving computing power allows to delineate reaction mechanisms in a step-by-step process, it is not only possible to take surface spin states into account but also absolutely necessary as this will affect reaction kinetics of pyrite oxidation as well as pyrite catalysis by orders of magnitude.

5 Conflicts of Interest

There are no conflicts to declare.

6 Acknowledgements

K.A. and D.R. are grateful for the support from the grants EAR1223976 and EAR1223600 from the National Science Foundation, while U.B.'s contribution was supported by the U.S. Office of Science, Basic Energy Sciences, Grant #DE-FG02-06ER15783. This research used computational resources of the National Energy Research Scientific Computing Center, a DOE Office of Science User Facility supported by the Office of Science of the U.S. Department of Energy under Contract No. DE-AC02-05CH11231.

7 References

1. A. Gartman, A. J. Findlay and G. W. Luther, *Chem. Geol.*, 2014, **366**, 32-41.

2. A. Gartman and G. W. Luther, *Abstracts of Papers of the American Chemical Society*, 2013, **245**.

3. A. Picard, A. Gartman, D. R. Clarke and P. R. Girguis, *Geochimica Et Cosmochimica Acta*, 2018, **220**, 367-384.

4. R. Guilbaud, I. B. Butler, R. M. Ellam and D. Rickard, *Earth and Planetary Science Letters*, 2010, **300**, 174-183.

5. Y. S. Han, T. J. Gallegos, A. H. Demond and K. F. Hayes, *Water Research*, 2011, **45**, 593-604.

6. Y. S. Han, H. Y. Jeong, A. H. Demond and K. F. Hayes, *Water Research*, 2011, **45**, 5727-5735.

7. R. Hough, M. Reich and R. Noble, *Noble Metal Nanoparticles in Ore Systems*2012.

8. R. M. Hough, R. R. P. Noble and M. Reich, *Ore Geology Reviews*, 2011, **42**, 55-61.

9. D. Rickard and G. W. Luther, *Chemical Reviews*, 2007, **107**, 514-562.

10. K. M. Rosso and D. J. Vaughan, eds., *Sulfide Mineralogy and Geochemistry*, Mineralogical Society of America, 2006.

11. S. Chaturvedi, R. Katz, J. Guevremont, M. A. A. Schoonen and D. R. Strongin, *American Mineralogist*, 1996, **81**, 261-264.

12. K. M. Rosso, U. Becker and M. F. Hochella, *American Mineralogist*, 2000, **85**, 1428-1436.

13. J. R. Mycroft, G. M. Bancroft, N. S. McIntyre, J. W. Lorimer and I. R. Hill, *Journal of Electroanalytical Chemistry*, 1990, **292**, 139-152.

14. H. W. Nesbitt, G. M. Bancroft, A. R. Pratt and M. J. Scaini, *American Mineralogist*, 1998, **83**, 1067-1076.

15. C. M. Eggleston, J. J. Ehrhardt and W. Stumm, *American Mineralogist*, 1996, **81**, 1036-1056.

16. C. M. Eggleston, J. J. Ehrhardt and W. Stumm, *Abstracts of Papers of the American Chemical Society*, 1997, **213**, 181-GEOC.

17. A. R. Elsetinow, J. M. Guevremont, D. R. Strongin, M. A. A. Schoonen and M. Strongin, *American Mineralogist*, 2000, **85**, 623-626.

18. J. M. Guevremont, A. R. Elsetinow, D. R. Strongin, J. Bebie and M. A. A. Schoonen, *American Mineralogist*, 1998, **83**, 1353-1356.

19. J. M. Guevremont, J. Bebie, A. R. Elsetinow, D. R. Strongin and M. A. A. Schoonen, *Environmental Science and Technology*, 1998, **32**, 3743-3748.

20. K. M. Rosso, U. Becker and M. F. Hochella, *American Mineralogist*, 1999, **84**, 1535-1548.

21. H. W. Nesbitt and I. J. Muir, *Geochimica et Cosmochimica Acta*, 1994, **58**, 4667-4679.

22. U. Becker, K. M. Rosso and M. F. Hochella, *Geochimica et Cosmochimica Acta*, 2001, **65**, 2641-2649.

23. D. Renock and U. Becker, *Geochimica et Cosmochimica Acta*, 2010, **74**, 4266-4284.

24. K. M. Rosso and U. Becker, *Geochimica et Cosmochimica Acta*, 2003, **67**, 941-953.

25. M. Sundararajan, R. S. Assary, I. H. Hillier and D. J. Vaughan, *Dalton Transactions*, 2011, **40**, 11156.

26. U. Becker, A. W. Munz, A. R. Lennie, G. Thornton and D. J. Vaughan, *Surface Science*, 1997, **389**, 66-87.

27. F. N. Skomurski, L. C. Shuller, R. C. Ewing and U. Becker, *J. Nucl. Mater.*, 2008, **375**, 290-310.

28. S. D. Taylor, M. C. Marcano, K. M. Rosso and U. Becker, *Geochimica et Cosmochimica Acta*, 2015, **156**, 154-172.

29. K. Arumugam and U. Becker, *Minerals*, 2014, **4**, 345-387.

30. D. R. Alfonso, *Journal of Physical Chemistry C*, 2010, **114**, 8971-8980.

31. U. Becker and M. F. Hochella, *Geochimica Et Cosmochimica Acta*, 1996, **60**, 2413-2426.

32. U. Becker, M. F. Hochella and E. Apra, *American Mineralogist*, 1996, **81**, 1301-1314.

33. U. Becker, M. F. Hochella and D. J. Vaughan, *Geochimica Et Cosmochimica Acta*, 1997, **61**, 3565-3585.

34. U. Becker, K. M. Rosso, R. Weaver, M. Warren and M. F. Hochella, *Geochimica Et Cosmochimica Acta*, 2003, **67**, 923-934.

35. J. Rakovan, U. Becker and M. F. Hochella, *American Mineralogist*, 1999, **84**, 884-894.

36. K. M. Rosso, U. Becker and M. F. Hochella, *American Mineralogist*, 1999, **84**, 1549-1561.

37. A. G. Berlich, H. W. Nesbitt, G. M. Bancroft and R. Szargan, *Surface Science*, 2013, **611**, 60-66.

38. H. W. Nesbitt, A. G. Berlich, S. L. Harmer, I. Uhlig, G. M. Bancroft and R. Szargan, *American Mineralogist*, 2004, **89**, 382-389.

39. H. W. Nesbitt, A. Schaufuss, M. Sciani, H. Hochst, G. M. Bancroft and R. Szargan, *Geochimica Et Cosmochimica Acta*, 2003, **67**, 845-858.

40. H. W. Nesbitt, A. G. Schaufuss, M. Scaini, G. M. Bancroft and R. Szargan, *American Mineralogist*, 2001, **86**, 318-326.

41. A. G. Schaufuss, H. W. Nesbitt, M. J. Scaini, H. Hoechst, M. G. Bancroft and R. Szargan, *American Mineralogist*, 2000, **85**, 1754-1766.

42. R. Poli and J. N. Harvey, *Chem. Soc. Rev.*, 2003, **32**, 1-8.

43. J. N. Harvey, *Physical Chemistry Chemical Physics*, 2007, **9**, 331-343.

44. K. P. Jensen and U. Ryde, *Journal of Biological Chemistry*, 2004, **279**, 14561-14569.

45. S. M. Walker, M. C. Marcano, W. M. Bender and U. Becker, *Chem. Geol.*, 2016, **429**, 60-74.

46. R. Prabhakar, P. E. M. Siegbahn, B. F. Minaev and H. Agren, *Journal of Physical Chemistry B*, 2004, **108**, 13882-13892.

47. M. Binetti, O. Weisse, E. Hasselbrink, A. J. Komrowski and A. C. Kummel, *Faraday Discussions*, 2000, **117**, 313-320.

48. A. J. Komrowski, J. Z. Sexton, A. C. Kummel, M. Binetti, O. Weisse and E. Hasselbrink, *Physical Review Letters*, 2001, **87**.

49. J. Behler, B. Delley, S. Lorenz, K. Reuter and M. Scheffler, *Physical Review Letters*, 2005, **94**.

50. A. L. Buchachenko and V. L. Berdinsky, *Journal of Physical Chemistry*, 1996, **100**, 18292-18299.

51. C. H. Ho, Y. S. Huang and K. K. Tiong, *Journal of Alloys and Compounds*, 2006, **422**, 321-327.

52. A. Ennaoui, S. Fiechter, C. Pettenkofer, N. Alonso-Vante, K. Büker, M. Bronold, C. Höpfner and H. Tributsch, *Solar Energy Materials and Solar Cells*, 1993, **29**, 289-370.

53. E. D. Stevens, M. L. DeLucia and P. Coppens, *Inorganic Chemistry*, 1980, **19**, 813-820.

54. M. S. Schmøkel, L. Bjerg, S. Cenedese, M. R. V. Jørgensen, Y.-S. Chen, J. Overgaard and B. B. Iversen, *Chemical Science*, 2014, **5**, 1408.

55. M. Bronold, Y. Tomm and W. Jaegermann, *Surface Science*, 1994, **314**, L931-L936.

56. H. W. Nesbitt, M. S. Caini, H. H. Öchst, G. M. B. Ancroft, A. G. S. Chaufuss and R. S. Zargan, *American Mineralogist*, 2000, **85**, 850-857.

57. G. U. von Oertzen, W. M. Skinner and H. W. Nesbitt, *Phys. Rev. B*, 2005, **72**, 10.

58. R. Sun, M. K. Y. Chan and G. Ceder, *Phys. Rev. B*, 2011, **83**, 235311.

59. Y. N. Zhang, J. Hu, M. Law and R. Q. Wu, *Physical Review B - Condensed Matter and Materials Physics*, 2012, **85**, 1-5.

60. G. U. von Oertzen, W. M. Skinner and H. W. Nesbitt, *Radiation Physics and Chemistry*, 2006, **75**, 1855-1860.

61. A. Hung, J. Muscat, I. Yarovsky and S. P. Russo, *Surface Science*, 2002, **513**, 511-524.

62. M. Bronold, C. Pettenkofer and W. Jaegermann, *Journal of Applied Physics*, 1994, **76**, 5800-5808.

63. J. S. Griffith, *Journal of Inorganic and Nuclear Chemistry*, 1956, **2**, 1-10.

64. R. G. Burns, *Mineralogical Applications of Crystal Field Theory*, Cambridge University Press, London, 1993.

65. A. Schlegel and P. Wachter, *J. Phys. C: Solid State Phys.*, 1976, **9**, 3363-3369.

66. A. D. Becke, *Physical Review A*, 1988, **38**, 3098-3100.

67. A. D. Becke, *The Journal of Chemical Physics*, 1993, **98**, 1372.

68. C. Lee, W. Yang and R. G. Parr, *Phys. Rev. B*, 1988, **37**, 785-789.

69. D. N. Bowman and E. Jakubikova, *Inorganic Chemistry*, 2012, **51**, 6011-6019.

70. J. P. Janet, L. Chan and H. J. Kulik, *Journal of Physical Chemistry Letters*, 2018, **9**, 1064-1071.

71. H. Paulsen, L. Duelund, H. Winkler, H. Toftlund and H. X. Trautwein, *Inorganic Chemistry*, 2001, **40**, 2201-2203.

72. F. Remacle, F. Grandjean and G. J. Long, *Inorganic Chemistry*, 2008, **47**, 4005-4014.

73. M. J. Frisch, G. W. Trucks, H. B. Schlegel, G. E. Scuseria, M. A. Robb, J. R. Cheeseman, G. Scalmani, V. Barone, B. Mennucci, G. A. Petersson, H. Nakatsuji, M. Caricato, X. Li, H. P. Hratchian, A. F. Izmaylov, J. Bloino, G. Zheng, J. L. Sonnenberg, M. Hada, M. Ehara, K. Toyota, R. Fukuda, J. Hasegawa, M. Ishida, T. Nakajima, Y. Honda, O. Kitao, H. Nakai, T. Vreven, J. A. Montgomery, Jr., J. E. Peralta, F. Ogliaro, M. Bearpark, J. J. Heyd, E. Brothers, K. N. Kudin, V. N. Staroverov, R. Kobayashi, J. Normand, K. Raghavachari, A. Rendell, J. C. Burant, S. S. Iyengar, J. Tomasi, M. Cossi, N. Rega, J. M. Millam, M. Klene, J. E. Knox, J. B. Cross, V. Bakken, C. Adamo, J. Jaramillo, R. Gomperts, R. E. Stratmann, O. Yazyev, A. J. Austin, R. Cammi, C. Pomelli, J. W. Ochterski, R. L. Martin, K. Morokuma, V. G. Zakrzewski, G. A. Voth, P. Salvador, J. J. Dannenberg, S. Dapprich, A. D. Daniels, Ö. Farkas, J. B. Foresman, J. V. Ortiz, J. Cioslowski and D. J. Fox, in *Gaussian, Inc., Wallingford CT,*2009.

74. A. E. Reed, L. a. Curtiss and F. Weinhold, *Chemical Reviews (Washington, DC, United States)*, 1988, **88**, 899-926.

75. A. Klamt and G. Schuurmann, *J. Chem. Soc., Perkin Trans. 2*, 1993, 799-805.

76. M. Cossi, N. Rega, G. Scalmani and V. Barone, *Journal of Computational Chemistry*, 2003, **24**, 669-681.

77. V. Barone and M. Cossi, *J. Phys. Chem. A*, 1998, **102**, 1995-2001.

78. G. Henkelman, A. Arnaldsson and H. Jónsson, *Computational Materials Science*, 2006, **36**, 354-360.

79. E. Sanville, S. D. Kenny, R. Smith and G. Henkelman, *Journal of computational chemistry*, 2007, **28**, 899-908.

80. W. Tang, E. Sanville and G. Henkelman, *Journal of Physics. Condensed Matter : an Institute of Physics Journal*, 2009, **21**, 084204.

81. Biovia, *Materials Studio v7.0.102*, 2013.

82. G. Kerr, D. Craw, D. Trumm and J. Pope, *Applied Geochemistry*, 2018, **97**, 123-133.

83. J. P. Perdew, K. Burke, M. Ernzerhof, D. of Physics and N. O. L. J. Quantum Theory Group Tulane University, *Physical Review Letters*, 1996, **77**, 3865-3868.

84. B. Delley, *Journal of Chemical Physics*, 2000, **113**, 7756-7764.

85. H. J. Monkhorst and J. D. Pack, *Phys. Rev. B*, 1976, **13**, 5188-5192.

86. L. G. Vanquickenborne and L. Haspeslagh, *Inorganic Chemistry*, 1982, **21**, 2448-2454.

87. J. Hu, Y. Zhang, M. Law and R. Wu, *Physical Review B - Condensed Matter and Materials Physics*, 2012, **85**, 1-10.

88. V. N. Antonov, L. P. Germash, A. P. Shpak and A. N. Yaresko, *Physica Status Solidi B-Basic Solid State Physics*, 2009, **246**, 411-416.

89. G. Z. Qiu, Q. Xiao, Y. H. Hu, W. Q. Qin and D. Z. Wang, *Journal of Colloid and Interface Science*, 2004, **270**, 127-132.

90. J. Majzlan, M. Chovan, P. Andras, M. Newville and M. Wiedenbeck, *Neues Jahrbuch Fur Mineralogie-Abhandlungen*, 2010, **187**, 1-9.

91. J. Xia, J. Jiao, B. Dai, W. Qiu, S. He, W. Qiu, P. Shen and L. Chen, *RSC Advances*, 2013, **3**, 6132.

92. G. Brostigen and A. Kjeksjus, *Acta Chem. Scand.*, 1969, **23**, 2186-2188.

93. R. Wu, Y. F. Zheng, X. G. Zhang, Y. F. Sun, J. B. Xu and J. K. Jian, *Journal of Crystal Growth*, 2004, **266**, 523-527.

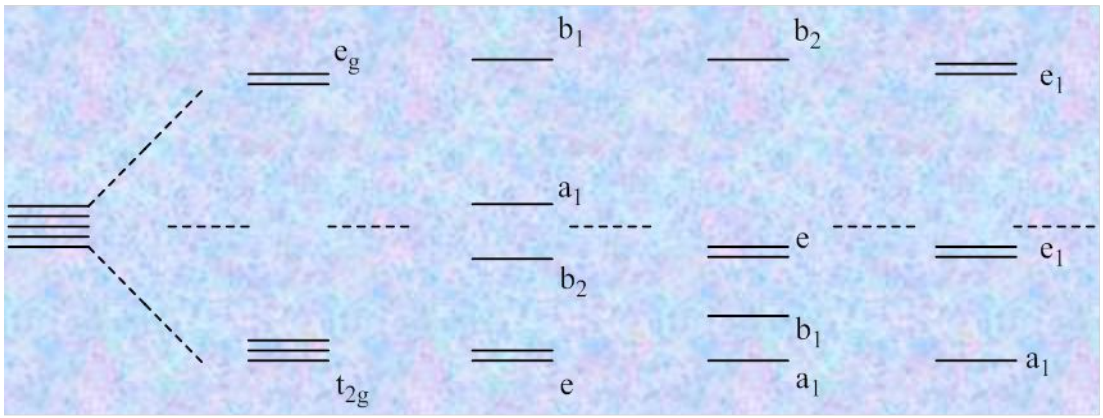

d-orbitals *[degenerate]*	O_h [CN=6]	C_{4v} [CN=5]	D_{2d} [CN=4]	C_{3v} [CN=3]
	$t_{2g}(d_{xy}$ & d_{xz} & $d_{yz})$	$e(d_{xz}$ & $d_{yz})$	$a_1(d_{z2})$	$a_1(d_{z2})$
	$e_g(d_{x2-y2}$ & $d_{z2})$	$b_2(d_{xy})$	$b_1(d_{x2-y2})$	$e_1(d_{xy}$ & $d_{x2-y2})$
		$a_1(d_{z2})$	$e(d_{xz}$ & $d_{yz})$	$e_1(d_{xz}$ & $d_{yz})$
		$b_1(d_{x2-y2})$	$b_2(d_{xy})$	

Schematic 1. Different local Fe environments and anticipated approximate d-orbital splitting patterns (CN refers to the local-coordination number of Fe-atom). Where a → symmetric w.r.t. the principle axis of rotation; b → Antisymmetric w.r.t. the principle axis of rotation; t → represents triply degenerate; e → represents doubly degenerate; and g → subscript represents the orbital is symmetric w.r.t. the center of symmetry or inversion (Mulliken symbol of irreducible representations). Different aspects of this Schematic are explained later in different sections throughout the text.

Figures

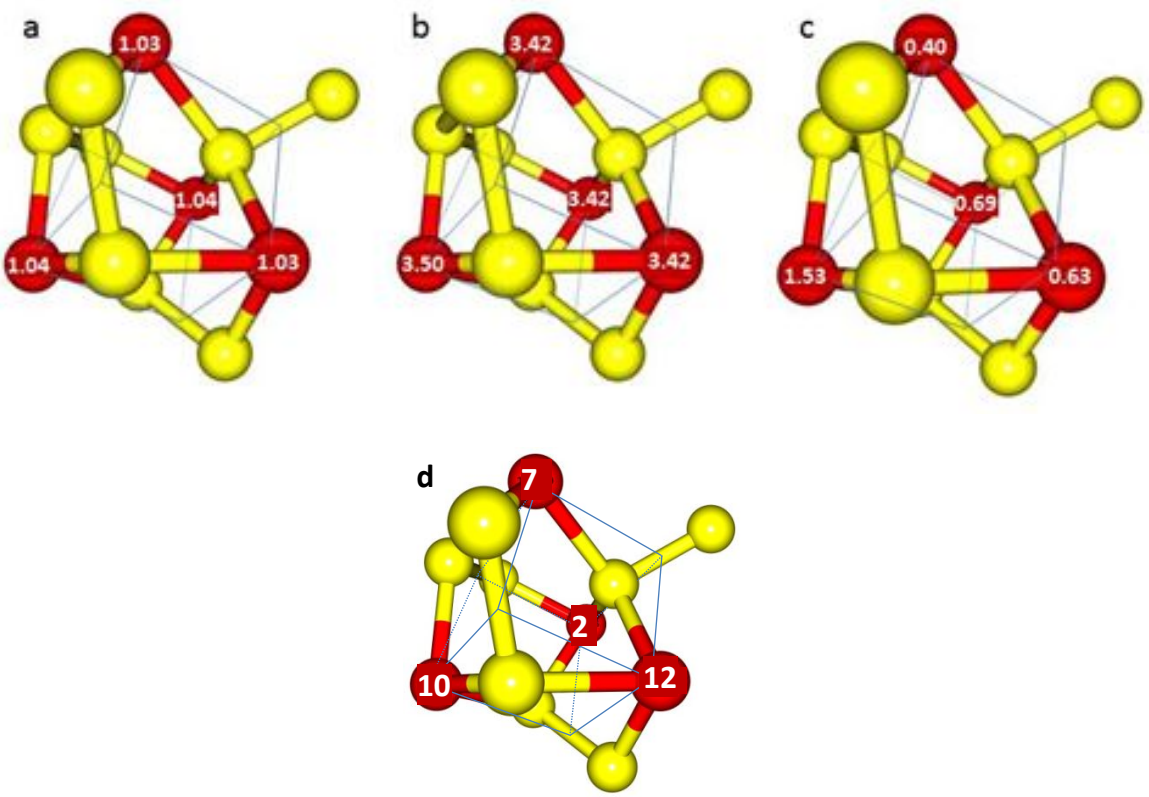

Figure 1. Pyrite Fe_4S_8 cluster model showing the (a) Bader charges (note that these charges reflect some of the covalent character and are therefore lower than the formal charge of +2) and (b) Bader spins, (c) CFSEs of the Fe atoms in eV, and (d) Fe-atoms with number labels. The drawn-in cubes represent the cubic character of this cluster if the centers of the disulfide groups are considered as one corner of such a cube.

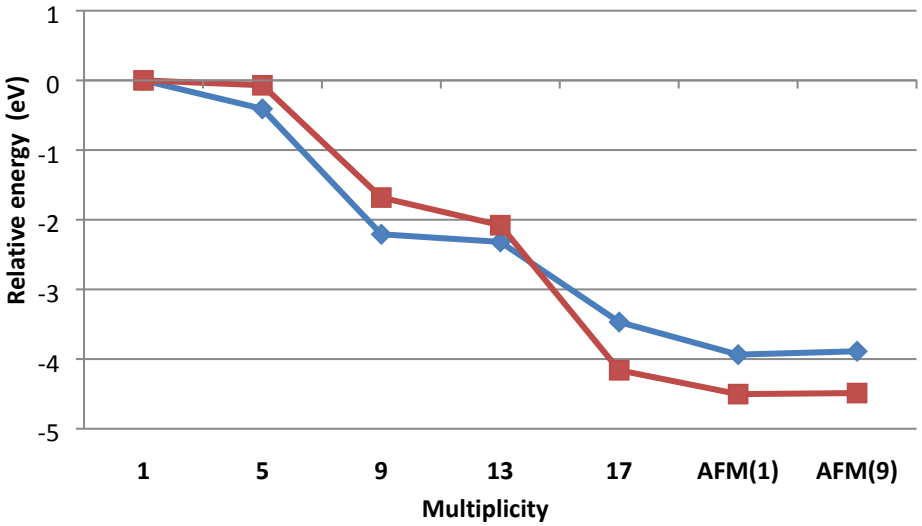

Figure 2. Relative energies (RE) of the pyrite Fe_4S_8 cluster model as a function of various possible overall spin multiplicities (spin multiplicity, M=2S+1, where S=n*(1/2), and n=number of unpaired electrons) (blue and red line correspond to calculations in vacuum and dielectric continuum, respectively). "1" is a low-spin calculation and all the numbers up to 17 (maximum number of four spins on each Fe(II)) have ferromagnetic ordering, while "AFM" represent two different antiferromagnetic ordering schemes described in the text. Since the Fe atom on the left is on the 3-fold axis and the other three off (symmetry equivalent), AFM(9) is the latter 3 Fe atoms with 4 up spins and the one on the left four down spins. The red line represents the computed REs in a Conductor-like Polarizable Continuum Model (CPCM) and the blue line represents the computed REs in the gas-phase.

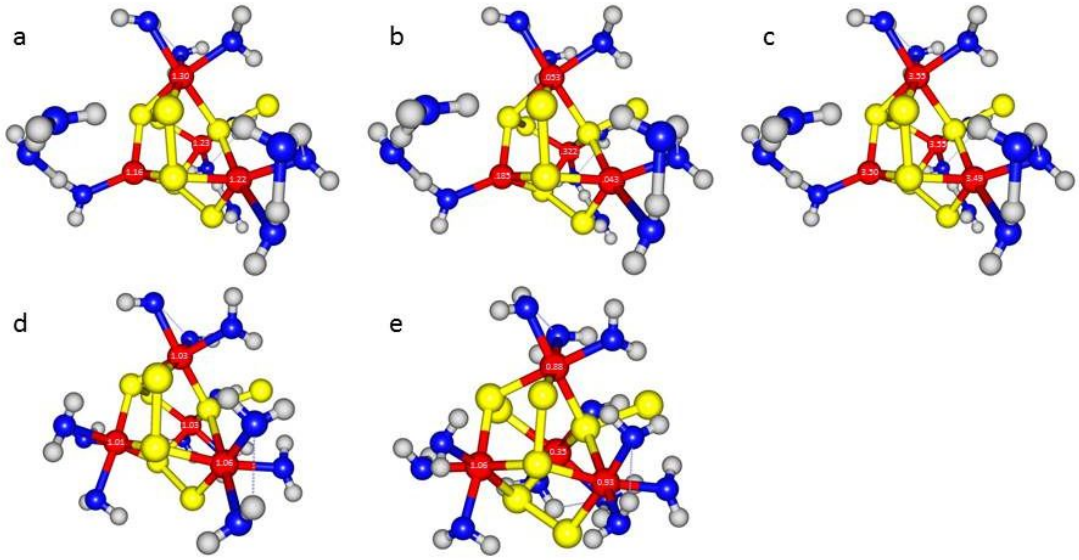

Figure 3. Fe_4S_8-clusters model with 12 geometry-optimized water molecules. The upper row (a-c) refers to the HS-FM state (a: Bader charges, b: CFSE in eV, c: Bader spin density) and the lower row to the LS-spin singlet state (d: Bader charges, e: CFSE in eV).

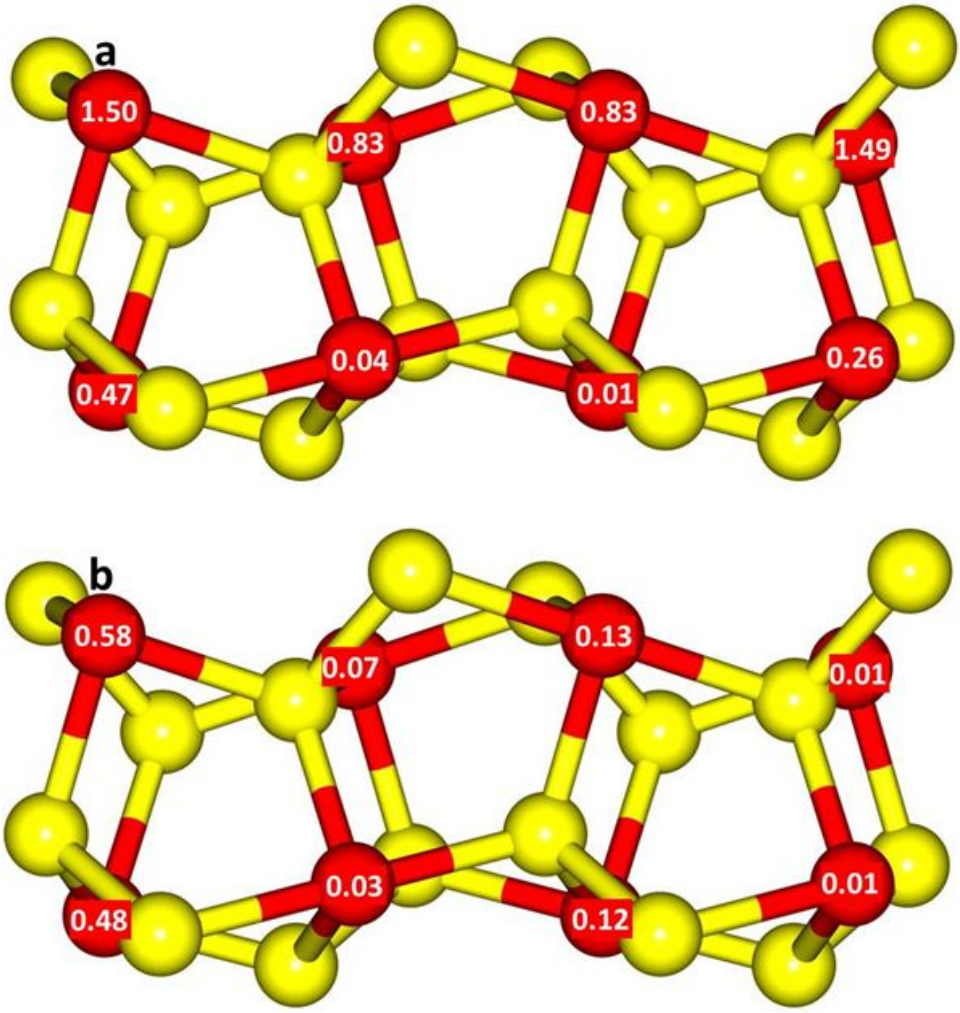

Figure 4. Fe_8S_{16} pyrite cluster model (side view) showing CFSEs calculated for the low-spin (LS) singlet state (a) and high-spin FM state corresponding to the spin multiplicity of 33 (b).

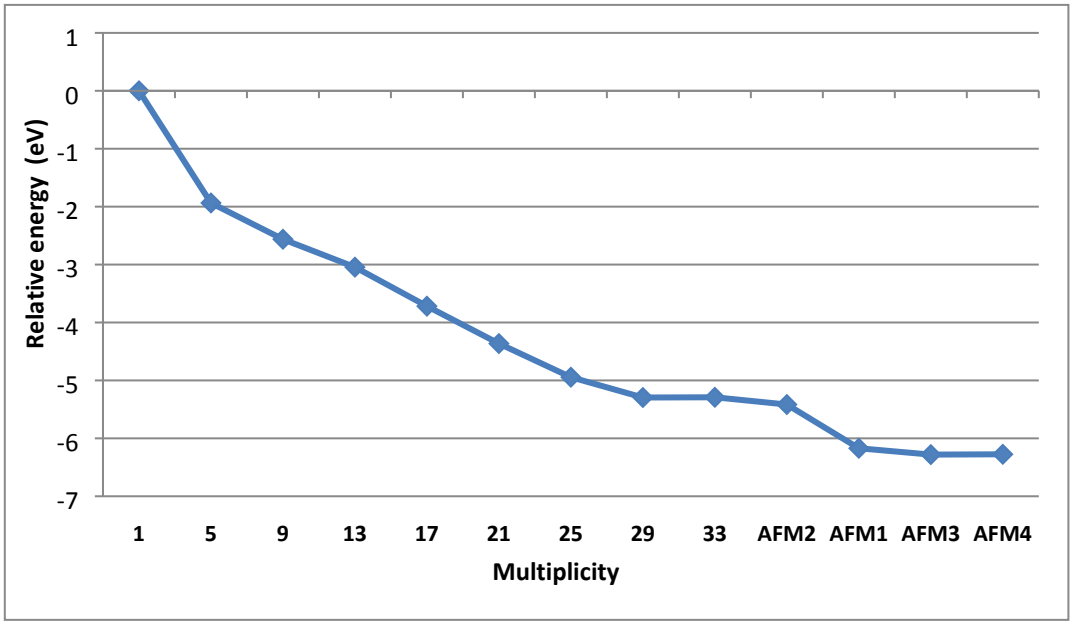

Figure 5. Relative energies of the pyrite Fe_8S_{16} cluster model as a function of various possible overall spin multiplicities (AFM refers to antiferromagnetic singlet states).

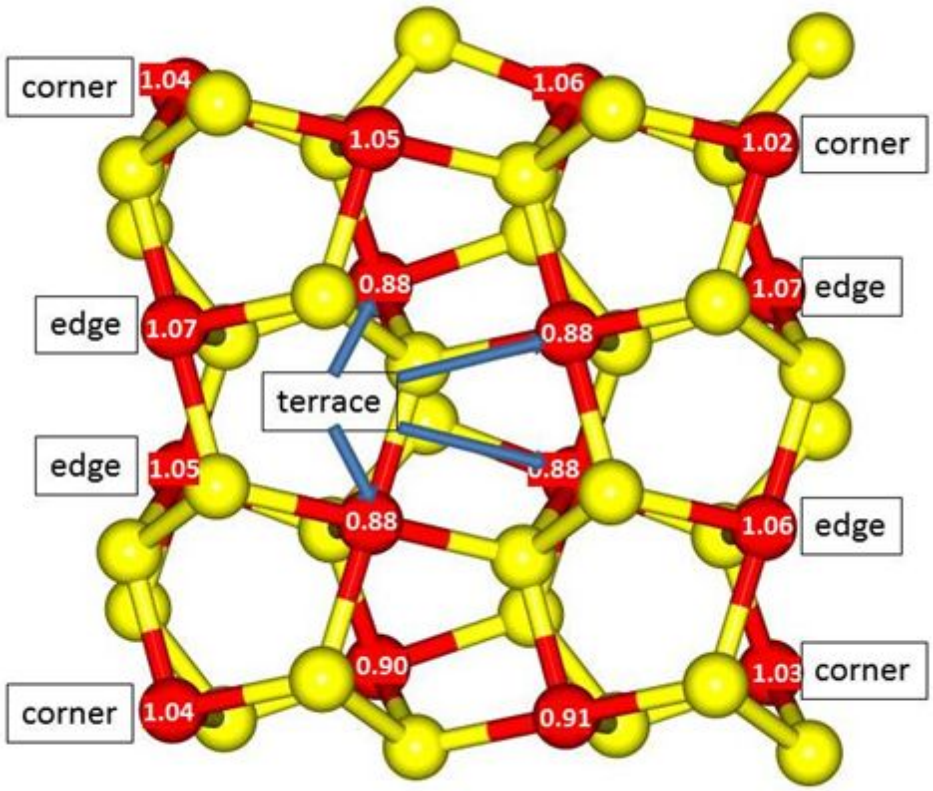

Figure 6. The $Fe_{16}S_{32}$ pyrite cluster model showing Bader charges calculated for the spin multiplicity of the entire cluster of 53.

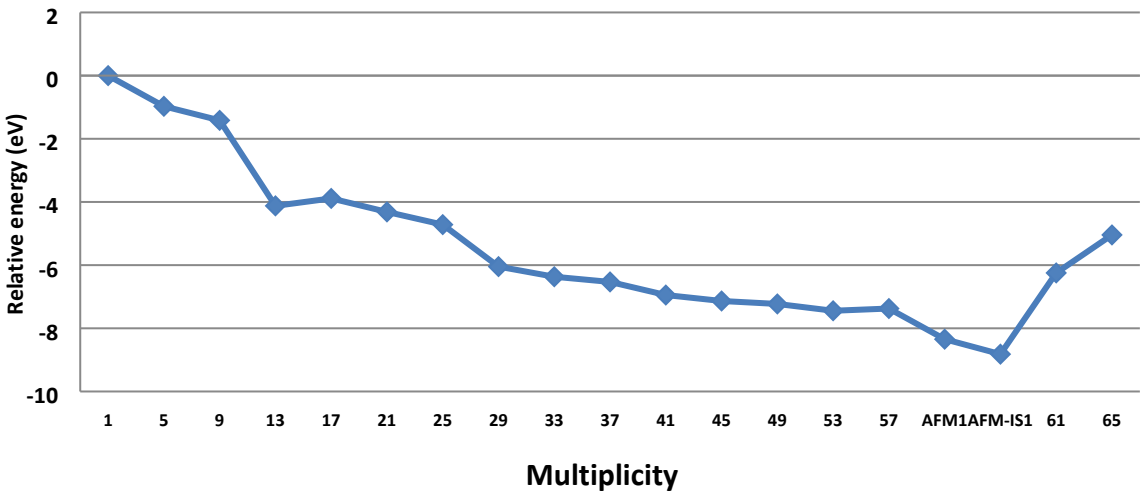

Figure 7. Relative energies of the pyrite $Fe_{16}S_{32}$ cluster model as a function of various possible overall spin multiplicities.

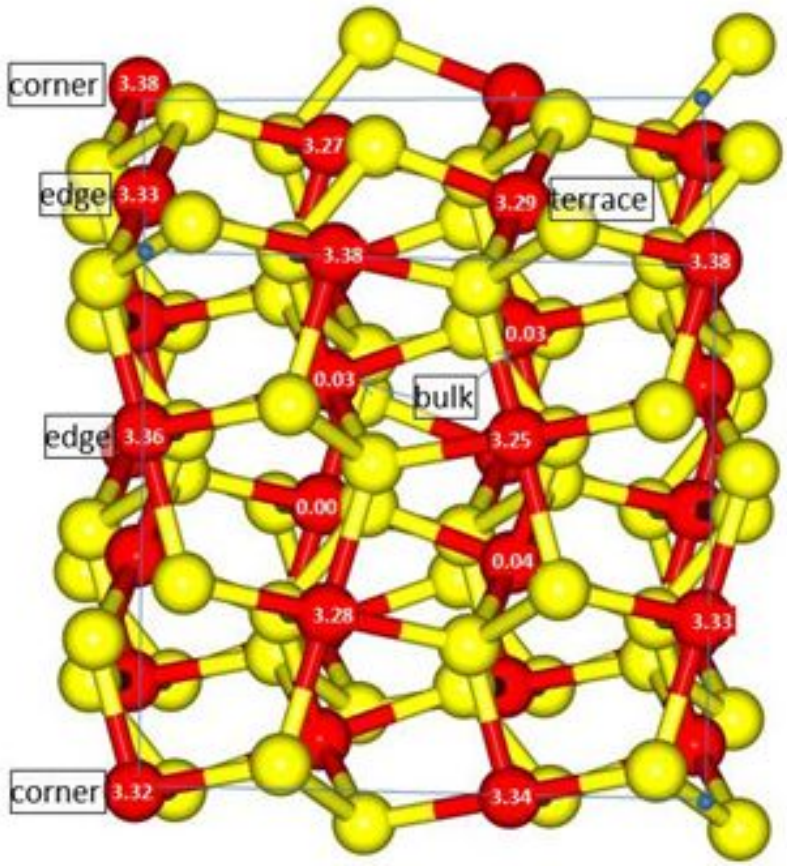

Figure 8. $Fe_{32}S_{64}$ cluster model showing Bader spins calculated for corner, edge, terrace, and bulk Fe(II) ions.

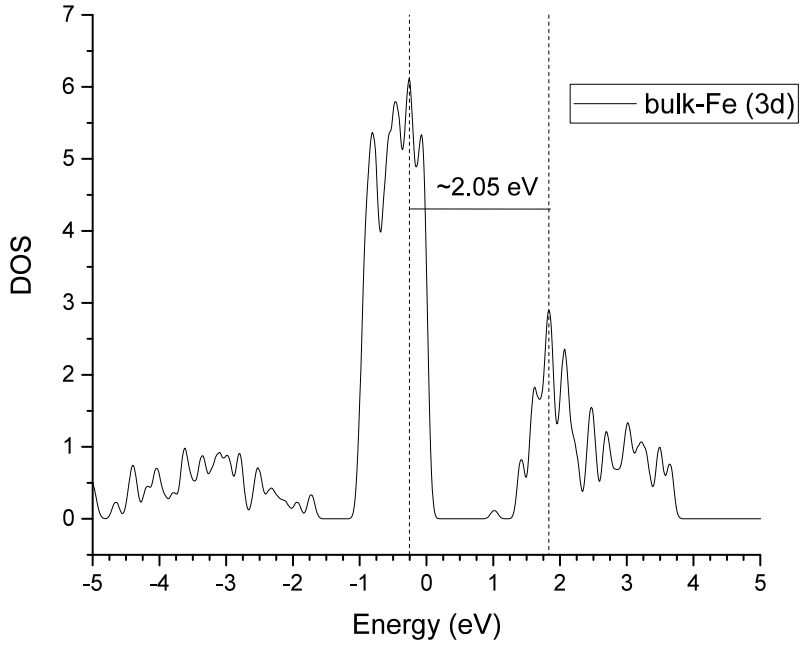

Figure 9. Partial density of states (PDOS) calculated for pyrite bulk Fe(II) 3d orbitals using CASTEP. The different peaks correspond to further splittings within the t_{2g} and e_{2g} sets. Rather than taking the difference between the edges (which is ~0.6 eV corresponds to the bulk band gap), taking the difference between maximum of peaks of the edge includes some amount of internal splitting energy to the overall splitting. The vertical lines correspond to the peak maxima. However, this is just an approximation.

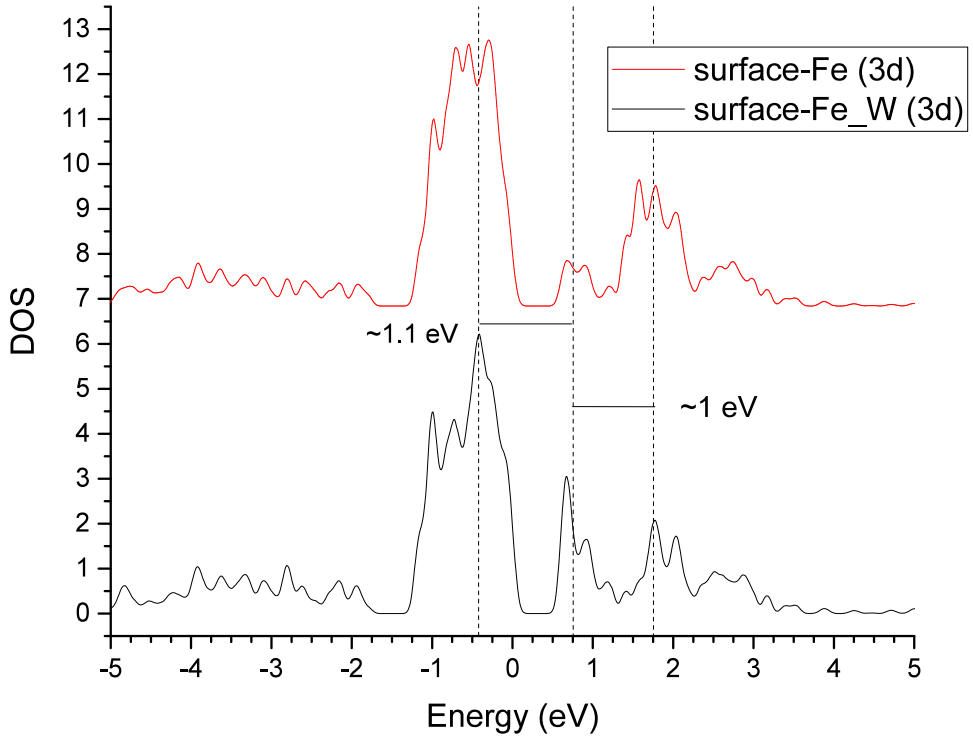

Figure 10. Partial DOS of pyrite(100) surface Fe 3d orbitals (surface-Fe(3d) refers to surface Fe(II) and surface-Fe_W(3d) refers to surface Fe(II) with an adsorbed water molecule). The three dashed vertical lines correspond to the peak maxima around the Fermi level. Generally, the band gap value is equal to the difference between the band edges of valence and conduction bands. However, due to the internal splitting of d-orbitals, further peaks appear in the PDOS profile (middle dashed line). Taking the difference between maximum of peaks of the edge includes some amount of internal splitting energy to the overall splitting (1.1+1 eV) which agrees with the overall crystal field splitting of bulk Fe(II) ion. This is just to demonstrate the fact that the internal splitting are prominent when it comes to surface or undercoordinated Fe(II) ions.

Tables

Table 1. Energies (in eV) of *d* orbitals and crystal field splitting energies (CFSE, last line) obtained for the singlet state of the Fe_4S_8 cluster model. The Fe atom labelled "12Fe" is on the 3-fold axis while Fe atoms 2, 7, and 10 are off the axis; however, the geometric symmetry equivalency is reduced by the electronic structure of the cluster.

2Fe		7Fe		10Fe*		12Fe	
Orbitals	eV	orbitals	eV	orbitals	eV	orbitals	eV
d_{yz}	-4.69	d_{xy}	-5.43	d_{xz}	-4.67	d_{xy}	-5.32
d_{x2-y2}	-5.65	d_{z2}	-5.69	d_{x2-y2}	-5.57	d_{yz}	-5.71
d_{xz}	-6.34	d_{yz}	-6.09	d_{z2}	-7.10	d_{xz}	-6.34
d_{xy}	-7.06	d_{x2-y2}	-6.65	d_{yz}	-7.19	d_{z2}	-6.37
d_{z2}	-7.14	d_{xz}	-7.01	d_{xy}	-7.47	d_{x2-y2}	-7.14
$d_{x2-y2} - d_{xz}$	0.69	$d_{z2} - d_{yz}$	0.40	$d_{x2-y2} - d_{z2}$	1.53	$d_{yz} - d_{xz}$	0.63

* this Fe(II) ion refers to the one lower left of Figure 1; this Fe is symmetrically different from the others as it is located on the three-fold symmetry axis.

Table 2. Energies of *d* orbitals and CFSEs (last line) obtained for the FM state (charge 0, multiplicity 17) of the Fe_4S_8 cluster model (eV).

2Fe		7Fe		10Fe		12Fe	
orbitals	eV	orbitals	eV	orbitals	eV	orbitals	eV
d_{x2-y2}	-10.29	d_{xz}	-9.81	d_{yz}	-10.18	d_{z2}	-10.03
d_{xz}	-10.39	d_{yz}	-10.22	d_{z2}	-10.92	d_{yz}	-10.05
d_{z2}	-10.46	d_{z2}	-10.37	d_{xz}	-11.38	d_{x2-y2}	-10.53
d_{xy}	-10.51	d_{xy}	-10.67	d_{x2-y2}	-11.38	d_{xz}	-10.69
d_{yz}	-10.53	d_{x2-y2}	-10.68	d_{xy}	-11.46	d_{xy}	-10.72
$d_{xz} - d_{z2}$	0.07	$d_{yz} - d_{z2}$	0.15	$d_{z2} - d_{xz}$	0.46	$d_{yz} - d_{x2-y2}$	0.48

Table 3. CFSEs of the Fe_4S_8 and Fe_4S_8-$(H_2O)_{12}$ models calculated for the LS singlet and HS-FM states (eV).

Fe(II)	Fe_4S_8		Fe_4S_8-$(H_2O)_{12}$	
	LS	HS-FM	LS	HS-FM
2Fe	$(d_{x2-y2} - d_{xz})$0.69	$(d_{xz} - d_{z2})$0.07	$(d_{xz} - d_{z2})$0.34(td)*	$(d_{yz} - d_{xy})$ 0.04
7Fe	$(d_{z2} - d_{yz})$ 0.39	$(d_{yz} - d_{z2})$0.15	$(d_{xy} - d_{x2-y2})$0.88	$(d_{yz} - d_{z2})$ 0.32
10Fe	$(d_{x2-y2} - d_{z2})$1.53	$(d_{z2} - d_{xz})$0.45	$(d_{xz} - d_{yz})$1.068	$(d_{xz} - d_{z2})$0.18
12Fe	$(d_{yz} - d_{xz})$0.63 $(d_{xz} - d_{z2})$0.03*	$(d_{yz} - d_{x2-y2})$0.48	$(d_{x2-y2} - d_{z2})$ 0.93	$(d_{xy} - d_{xz})$0.05

*refers to the tetrahedral splitting order, but these Fe(II) atoms still show splitting with in the t_{2g} and e_g sets.

Table 4. CFSEs of Fe(II) ions of the Fe_8S_8 cluster calculated for the LS singlet and HS-FM state configurations (eV).

Fe_8S_{16}	LS		HS (all Fe)
2Fe (corner)	0.26[$d_{yz}-d_{z2}$]	d_{z2} lowered	0.014[$d_{z2}-d_{xy}$]
3Fe (corner)	1.49[$d_{x2-y2}-d_{xz}$]	O_h	0.005[$d_{xy}-d_{x2-y2}$]
6Fe (corner)	0.46[$d_{yz}-d_{z2}$]	d_{z2} lowered	0.48 [$d_{xz}-d_{z2}$]*
8Fe (corner)	1.50[$d_{x2-y2}-d_{xy}$]	O_h	0.58[$d_{xz}-d_{x2-y2}$]**
1Fe (edge)	0.04[$d_{yz}-d_{z2}$]	d_{z2} lowered	0.03[$d_{z2}-d_{xy}$]
4Fe(edge)	0.83[$d_{x2-y2}-d_{xy}$]	O_h $d_{z2}-d_{x2-y2}$ =0.7	0.07[$d_{x2-y2}-d_{xy}$]
5Fe(edge)	0.11[$d_{yz}-d_{z2}$]	d_{z2} lowered	0.12[$d_{xy}-d_{xz}$]
7Fe(edge)	0.83[$d_{x2-y2}-d_{xy}$]	O_h $d_{z2}-d_{x2-y2}$ =0.7	0.131[$d_{xy}-d_{xz}$]

* d_{z2} and d_{x2-y2} are lowered in energy and the d_{xy} is destabilized and the highest in energy and e_g orbitals are almost degenerate. ** the d_{x2-y2} orbital is lowered in energy than the almost degenerate d_{yz} and d_{xz}; the d_{z2} is the highest in energy.

Table 5. CFSEs (eV) of Fe(II) ions of the $Fe_{16}S_{32}$ cluster calculated using the B3LYP functional and calculated unpaired electron Mulliken spin density values (SM=1, 53, and 57).

$Fe_{16}S_{32}$	LS	52 unpaired spins		56 unpaired spins	
	CFSE/eV	CFSE/eV	spin	CFS/eVE	spin
4Fe (corner)	1.34 [$d_{x2-y2}-d_{yz}$]	0.07 [$d_{yz}-d_{z2}$]	3.42	0.14 [$d_{xy}-d_{z2}$]	3.42
5Fe (corner)	1.39 [$d_{x2-y2}-d_{xz}$]	0.14 [$d_{x2-y2}-d_{xy}$]	3.42	0.05 [$d_{x2-y2}-d_{xy}$]	3.43
10Fe (corner)	0.93 [$d_{x2-y2}-d_{xy}$]	0.24 [$d_{x2-y2}-d_{xy}$]	3.49	0.31 [$d_{z2}-d_{x2-y2}$]	3.51
16Fe (corner)	1.14 [$d_{z2}-d_{xz}$]	0.17 [$d_{yz}-d_{xz}$]	3.42	0.18 [$d_{yz}-d_{xz}$]	3.42
1Fe (edge)	0.92 [$d_{z2}-d_{yz}$]	0.002 [$d_{z2}-d_{xy}$]	3.51	0.04 [$d_{z2}-d_{xy}$]	3.52
3Fe (edge)	1.06 [$d_{x2-y2}-d_{xy}$]	0.03 [$d_{yz}-d_{x2-y2}$]	3.39	0.03 [$d_{yz}-d_{x2-y2}$]	3.39
6Fe (edge)	0.77 [$d_{x2-y2}-d_{xy}$]	0.23 [$d_{yz}-d_{xy}$]	**2.28**	0.09 [$d_{xy}-d_{xz}$]	3.48
7Fe (edge)	0.85 [$d_{z2}-d_{yz}$]	0.12 [$d_{xz}-d_{yz}$]	3.45	0.14 [$d_{xz}-d_{yz}$]	3.44
9Fe (edge)	0.94 [$d_{x2-y2}-d_{xy}$]	0.02 [$d_{yz}-d_{z2}$]	**2.29**	0.28 [$d_{xy}-d_{yz}$]	3.42
12Fe (edge)	0.93 [$d_{z2}-d_{xz}$]	0.20 [$d_{z2}-d_{xz}$]	3.49	0.09 [$d_{z2}-d_{xy}$]	3.49
14Fe (edge)	1.18 [$d_{z2}-d_{yz}$]	0.03 [$d_{xz}-d_{yz}$]	3.35	0.07 [$d_{xz}-d_{yz}$]	3.37
15Fe (edge)	0.81 [$d_{x2-y2}-d_{xy}$]	0.006 [$d_{yz}-d_{z2}$]	3.530	0.00 [$d_{yz}-d_{z2}$]	3.53
2Fe (surface)	0.86 [$d_{z2}-d_{yz}$]	0.17 [$d_{yz}-d_{x2-y2}$]	**2.20**	0.013 [$d_{x2-y2}-d_{yz}$] –O_h (0.41 [$d_{z2}-d_{x2-y2}$])	**2.16**
8Fe (surface)	0.88 [$d_{z2}-d_{yz}$]	0.045 [$d_{yz}-d_{x2-y2}$]	**2.38**	0.06 [$d_{yz}-d_{x2-y2}$]	**2.37**
11Fe (surface)	0.84 [$d_{z2}-d_{yz}$]	0.009 [$d_{yz}-d_{x2-y2}$]	**2.23**	0.01 [$d_{yz}-d_{x2-y2}$]	**2.23**
13Fe (surface)	0.92 [$d_{z2}-d_{yz}$]	0.013 [$d_{x2-y2}-d_{yz}$] –O_h (0.31 [$d_{z2}-d_{x2-y2}$])	**2.24**	0.023 [$d_{x2-y2}-d_{yz}$] –O_h (0.25 [$d_{z2}-d_{x2-y2}$])	**2.24**

* For the LS singlet state, all the Fe(II) show an O_h splitting pattern.

Table 6. CFSEs (eV) calculated for the Fe(II) ions of the $Fe_{32}S_{64}$ cluster corresponding to the AFM spin configurations and Mulliken unpaired electron spin density values.

$Fe_{32}S_{64}$	AFM state with 9 unpaired spins		AFM state with 5 unpaired spins	
	CFSE	spin	CFSE	Spin
6Fe (corner)	0.12 [d_{z2} –d_{x2-y2}]	3.342	0.12 [d_{xy} –d_{xz}]	3.38
12Fe (corner)	0.24 [d_{x2-y2} –d_{xz}]	3.372	0.88 [d_{x2-y2} –d_{yz}] –O_h 0.05 [d_{z2} –d_{x2-y2}] 0.85 [d_{xz} –d_{xy}]	3.38
75Fe (corner)	0.04 [d_{x2-y2} –d_{yz}]	3.380	0.14 [d_{x2-y2} –d_{xz}] –O_h 0.50[d_{z2} –d_{x2-y2}]	3.39
81Fe (corner)	0.10 [d_{xz} –d_{xy}]	3.389	0.82 [d_{z2} –d_{yz}]	3.39
17Fe (edge)	0.17 [d_{x2-y2} –d_{xz}] –O_h 0.12 [d_{z2} –d_{x2-y2}] 1.34 [d_{yz} –d_{xy}]	3.186	0.43 [d_{x2-y2} –d_{xz}]	3.19
18Fe (edge)	0.09 [d_{xz} –d_{xy}]	3.264	0.84 [d_{z2} –d_{xz}]	3.24
42Fe (edge)	0.23 [d_{z2} –d_{yz}]	3.184	0.16 [d_{xy} –d_{xz}]	3.19
51Fe (edge)	0.024 [d_{xz} –d_{xy}]	3.257	0.02 [d_{yz} –d_{xy}]	3.23
62Fe (edge)	0.074 [d_{x2-y2} –d_{xy}] –O_h 0.83 [d_{z2} –d_{x2-y2}]	3.402	0.30 [d_{yz} –d_{z2}]	3.43
66Fe (edge)	0.15 [d_{z2} –d_{xz}] –O_h 0.75 [d_{x2-y2} –d_{z2}]	3.337	0.44 [d_{x2-y2} –d_{yz}]	3.32
72Fe (edge)	0.76 [d_{x2-y2} –d_{xy}] –O_h 0.13 [d_{z2} –d_{x2-y2}]	3.400	0.20 [d_{z2} –d_{yz}]	3.44
78Fe (edge)	0.14 [d_{x2-y2} –d_{xy}]	3.34	0.35 [d_{xy} –d_{xz}]	3.32
82Fe (edge)	0.04 [d_{z2} –d_{yz}] –O_h 0.25 [d_{x2-y2} –d_{z2}] 1.89 [d_{xz} –d_{xy}]	3.17	0.34 [d_{x2-y2} –d_{yz}]	3.18
83Fe (edge)	0.24 [d_{xy} –d_{xz}]	3.41	0.51 [d_{z2} –d_{xz}]	3.43
93Fe (edge)	0.024 [d_{yz} –d_{xz}]	3.33	0.43 [d_{xz} –d_{yz}]	3.33
94Fe (edge)	0.34 [d_{yz} –d_{x2-y2}]	3.26	0.06 [d_{z2} –d_{xz}] –O_h 0.79 [d_{x2-y2} –d_{z2}]	3.23
28Fe (surface)	0.15 [d_{xy} –d_{yz}]	3.31	0.71 [d_{x2-y2} –d_{yz}]	2.02
40Fe (surface)	0.19 [d_{xz} –d_{yz}]	3.30	0.81 [d_{yz} –d_{z2}]	1.91
41Fe (surface)	0.33 [d_{xy}–d_{x2-y2}]	**2.05**	0.34 [d_{x2-y2} –d_{xy}]	2.02
49Fe (surface)	0.39 [d_{x2-y2} –d_{xz}]	3.18	0.11 [d_{xy} –d_{x2-y2}]	1.96
52Fe (surface)	0.02 [d_{z2} –d_{xz}]	**1.99**	0.31 [d_{xz} –d_{x2-y2}] –T_d order [4 sets, d_{z2} and d_{x2-y2}, d_{xz}, d_{yz}, d_{xy}]	1.99
58Fe (surface)	0.13 [d_{yz} –d_{z2}]	3.34	0.10 [d_{yz} –d_{x2-y2}]	2.05
61Fe (surface)	0.08 [d_{x2-y2} –d_{z2}]	3.32	1.62 [d_{x2-y2} –d_{z2}]	1.90
64Fe (surface)	0.06 [d_{x2-y2} –d_{z2}]	3.32	0.04 [d_{x2-y2} –d_{yz}] –O_h 0.12 [d_{z2} –d_{x2-y2}]	2.09
76Fe (surface)	0.49 [d_{yz} –d_{xz}]	3.29	1.31 [d_{yz}–d_{z2}]	1.92
80Fe (surface)	0.22 [d_{z2} –d_{xy}]	3.32	0.14 [d_{z2} –d_{x2-y2}]	2.07
87Fe (surface)	0.75 [d_{xy} –d_{yz}]	3.33	1.11 [d_{xy} –d_{x2-y2}]	2.00
90Fe (surface)	0.48 [d_{x2-y2} –d_{xz}]	3.16	0.69 [d_{yz} –d_{xz}]	1.97
50Fe (bulk)	0.30 [d_{xy} –d_{z2}]	0.47	0.20 [d_{xy} –d_{x2-y2}]	0.34
63Fe (bulk)	0.93 [d_{xz} –d_{x2-y2}]	0.44	0.01 [d_{xy} –d_{x2-y2}] –T_d order [3 sets, d_{z2}, d_{x2-y2} and d_{xy}, d_{xz} and d_{yz}]	0.39
67Fe (bulk)	0.48 [d_{yz} –d_{z2}]	0.36	0.60[d_{yz} –d_{z2}]	0.34
96Fe (bulk)	0.85 [d_{xz} –d_{z2}]	0.37	0.77 [d_{xz} –d_{z2}]	0.35

Table 7. Relative energies (eV) of pyrite fragments of molecular formula, FeS_n (n=6, 5, 4, and 3) with respect to the corresponding LS state.

Fragment	Relative energies		
	LS	HS	IS
FeS_6	0	0.49	0.43
FeS_5	0	0.05	0.23
FeS_4	0	–0.46	0.13
FeS_3	0	–0.57	–0.26)

Table 8. CFSE values calculated for the pyrite (FeS_n, n=6, 5, 4, and 3) fragments (eV).

FeS_n	***d*-orbitals splitting energy**		
	HS	**LS**	**IS**
FeS_6	0.15 [d_{xz}–d_{x2-y2}]	0.02 [d_{xy}–d_{x2-y2}]	0.41 [d_{xz}–d_{xy}]
FeS_5	0.17 [d_{z2}–d_{x2-y2}]	0.32 [d_{yz}–d_{x2-y2}]	0.18 [d_{z2}–d_{x2-y2}]
FeS_4	0.28 [d_{xz}–d_{x2-y2}]	0.25 [d_{xy}–d_{z2}]	0.08 [d_{z2}–d_{x2-y2}]
FeS_3	0.28 [d_{x2-y2}–d_{z2}]	0.91 [d_{x2-y2}–d_{z2}]	0.25 [d_{z2}–d_{yz}]

Table 9. Geometrical parameters computed at the GGA (PBE) method using the DMol^3, CASTEP codes, previous computational results, and experimental values.

	a/Å	S-S/Å	Fe-S/Å
Expt. [92]	5.42	2.18	2.26
Expt. [93]	5.42	-	-
Expt. [93]	5.41	2.12	-
Expt. [54]	5.42	2.16	2.26
w2k (PBE) [54]		2.16	2.26
This study/DMol^3	5.47	2.18	2.29
This study/CASTEP	5.40	2.18	2.26
LDA [58]	5.29	-	-
AM05 [58]	5.32	-	-
AM05+U [58]	5.33	-	-
PBE [58]	5.40	-	-
PBE+U [58]	5.42	-	-

Table 10. Bandgap (eV) values of bulk pyrite and various surfaces.

Models	Bandgap (eV)	
	CASTEP	DMol^3
Pyrite (bulk)	0.58	0.95
Pyrite(100)-HSfix	Conductor	1.16
Pyrite(100)/AFM (energy)	0.54	1.04
Pyrite(100)/AFM (opt)	0.71	1.25
Pyrite(100) + 1 water	0.59	1.13
Pyrite(100)+1 water (AFM)	0.90	1.29
Pyrite(100) + water to all Fe(II)/HS	1.29	1.68

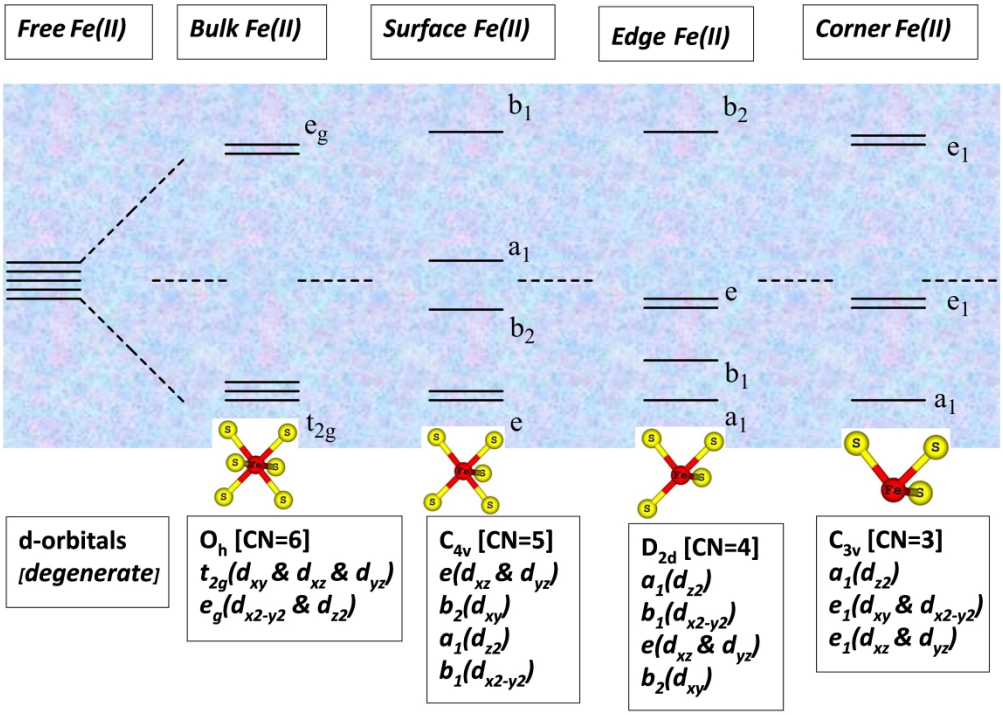

1300x921mm (96 x 96 DPI)